A Novel Method of Crystal Structure Analysis Using *In-Situ* Diffraction Measurement of Magnetically Oriented Microcrystal Suspension

2014

Kenji MATSUMOTO

Contents

General Introduction

1. Background

Biomass has been considered a viable solution to resource and energy problems in recent years. Biomass is used in various sizes; that is, by fragmentation into its constituent elements and used for fuel[1,2] or chemical products,[3,4] or by fragmentation into nanosized particles and used as a nanomaterial.[5,6] There are physical, chemical, and biochemical methods involved in the material conversion of biomass, but the biochemical method, particularly, conversion of biomass using enzyme reactions, is the one with good characteristics and compatibility.[7] However, because there are various problems with the practical use of enzyme activity and heat tolerance, improving the activation and heat tolerance of enzymes[8,9] becomes an important issue. Hence, information about the higher-order structure of enzymes is very important, as it has been used for the first time to improve the enzyme characteristics and ensure reaction control.[10] In addition, not only the structural information of the enzyme, but also that of the substrate on which it acts is important. Because the enzyme reaction is known, the steric structure of both the enzyme and the substrate can be understood for the first time. Furthermore, information on the structural connection between the enzyme and the substrate is important.[11,12]

The most common method to evaluate the structure of the enzyme and the substrate is **crystal structure analysis**, and the most commonly used means of crystal structure analysis is single-crystal X-ray diffraction (XRD) measurement.[13-15] However, a single crystal of at least 50 μm is required for the measurement, and many enzymes (proteins) and substrates do not grow to the sufficient size for single-crystal

structure analysis.[16] As a result, the analysis relies on XRD measurement of a powder sample (microcrystalline powder).[17,18] However, information related to diffraction is very limited for powder samples. Figure 1 shows a diagram of L-alanine monocrystal and powder XRD to explain the difference. The diffraction peak becomes a spot for a single crystal, from whose position the information of the diffraction plane is obtained. However, because the microcrystals are oriented in various directions in a powder sample, the diffraction image is in the form of a ring. It is difficult to determine the diffraction plane from this ring-shaped diffraction pattern, and because rings often overlap, the assignment of the peak is often difficult.[17] As a result, the promptness and accuracy of crystal structure analysis are inferior for powder samples as compared to those for single-crystal samples. In order to solve this, we propose a three-dimensional (3D) orientation of microcrystals using a magnetic field.

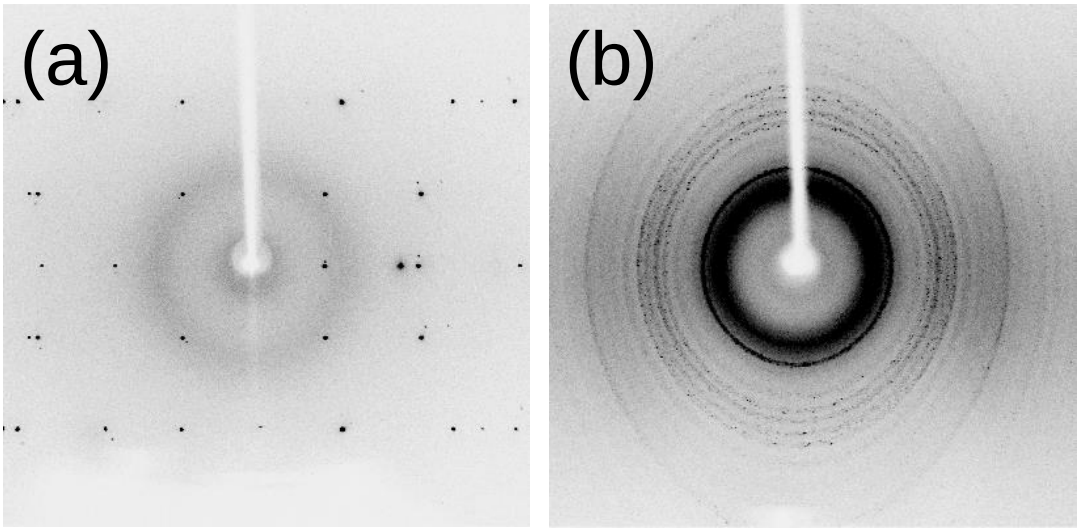

Figure 1. X-ray diffraction images of (a) a single crystal and (b) a microcrystalline powder of L-alanine. The diffraction peaks appear as spots for a single crystal and as rings for a microcrystalline powder.

2. Magnetic Orientation of Crystals and MOMA Method

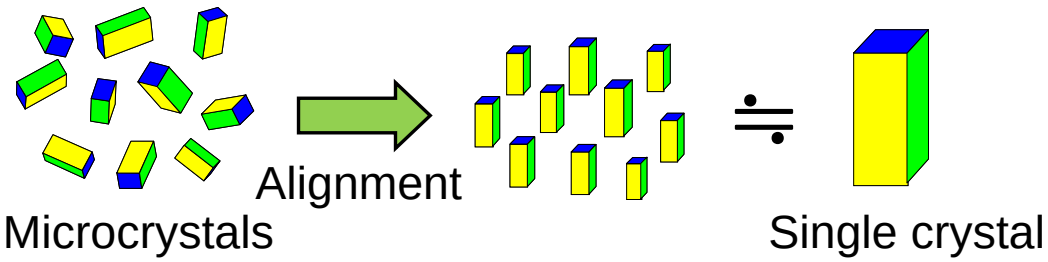

Figure 2. Three-dimensional alignment of a microcrystalline powder.

The main problem associated with powder X-ray structure analysis is that the microcrystals randomly orient in powder samples. If the microcrystal orientation in the powder can be restricted three-dimensionally, it is possible to obtain diffraction images similar to those from a single crystal (Figure 2).[19] A powerful technique to align microcrystals is magnetic orientation.[20-22] Magnetic orientation is applicable to all materials with magnetic anisotropy.[23] Because most organic crystals show magnetic anisotropy, it is possible to align them using a magnetic field.[24-26] Particularly, many biaxial organic crystals (triclinic, monoclinic, and orthorhombic crystals) have three different values of magnetic susceptibility ($\chi_1 > \chi_2 > \chi_3$) as shown in Figure 3, and the magnetic response is different for each of the three orthogonal directions. This suggests that three-dimensional orientation of biaxial crystals is possible by application of a magnetic field having different strengths three dimensionally.[19]

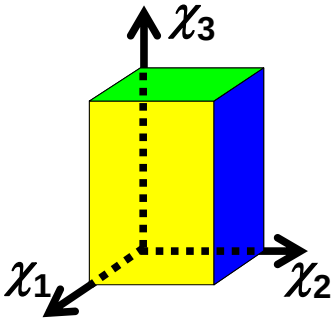

Figure 3. Magnetic susceptibility of a biaxial crystal.

We now explain magnetic field orientation of biaxial crystals in greater detail. If a static magnetic field is applied to a biaxial crystal, the χ_1 axis (the easy magnetization axis) of the microcrystal is in uniaxial orientation with the direction of the magnetic field, but the χ_2 and χ_3 axes cannot be fixated (Figure 4a).[19] However, if a fast rotating magnetic field is applied to a biaxial crystal, the χ_3 axis of the microcrystal (the hard magnetization axis) aligns in uniaxial orientation with the direction of the rotation axis, but the χ_1 and χ_2 axes cannot be fixated (Figure 4b).[19]

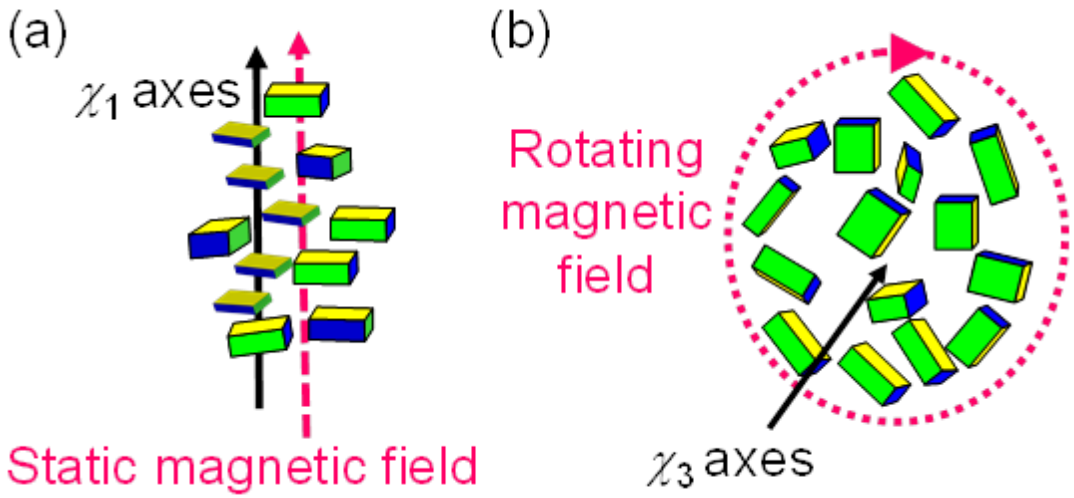

Figure 4. The uniaxial alignment of microcrystals. (a) Only χ_1 axes of microcrystals align in a static magnetic field. (b) Only χ_3 axes of microcrystals align in a rotating magnetic field.

If these two magnetic field orientations are well combined, though, a 3D orientation of the microcrystal can be obtained.[19,27] There are various methods to do this,[28] but we would like to introduce two typical methods. The first is a time-modulated rotating magnetic field (Figure 5).[28-30] This is basically a fast rotating magnetic field, but the rotation speed changes periodically. As shown in Figure 5, 0 º to α º and 180º to 180º+α º are low-speed ω_s, and α º to 180º and 180º+α º to 360º are

high-speed ω_q ($\omega_s<\omega_q$). If they are continuously rotated, a strong magnetic field appears in the direction of $\alpha/2$. The χ_1 axis aligns in the direction of the strongest magnetic field and the χ_3 axis aligns in the direction perpendicular to the rotation plane. As a result, 3D orientation of biaxial crystals becomes possible.

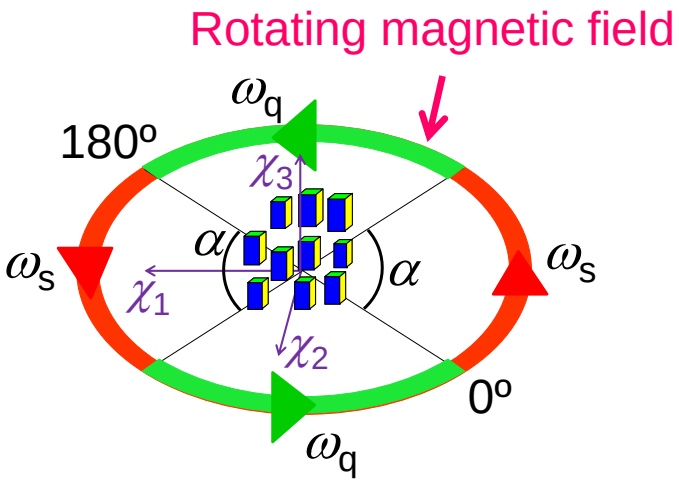

Figure 5. Schematic of time-dependent elliptic magnetic field. The magnetic field rotates at a speed of ω_s from 0º to α º and from 180º to 180º+α º. On the other hand, the magnetic field rotates at a speed of ω_q from α º to 180º and from 180º+ α º to 360º. The χ_1 axes of microcrystals orient to the direction of α º/2. On the other hand, the χ_3 axes of microcrystals orient to the direction of the rotating axis.

Another method for magnetic orientation of biaxial crystals is the intermittent rotation of the magnetic field (Figure 6).[28,31] This method uses a repeating 180º high-speed rotation with a break of time t_s. Because a strong magnetic field also appears in the direction of the break in this method, the χ_1 axis is aligned in the direction of the strong magnetic field, and the χ_3 axis is aligned in the direction of the rotation axis. As a result, 3D orientation becomes possible.

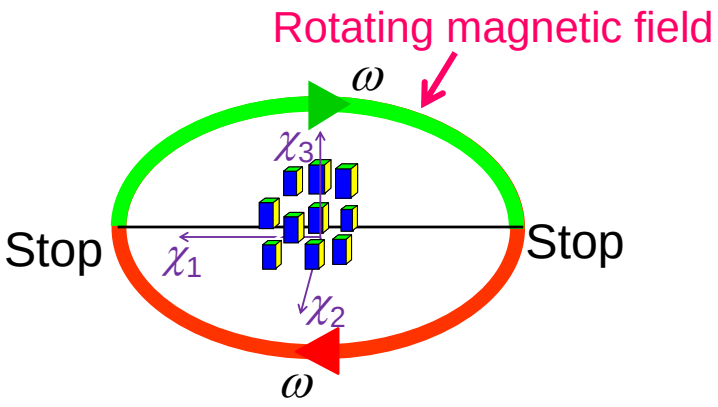

Figure 6. Schematic of intermittent rotating magnetic field, which is a repetition of a stop (duration of t_{stop}) and a 180° rotation (duration of t_{rot} at rotation speed of ω). The χ_1 axes of microcrystals orient to the stopping direction. On the other hand, the χ_3 axes of microcrystals orient to the direction of the rotating axis.

In order to conduct X-ray crystal structure analysis of 3D-oriented microcrystals, a fixation method using UV-curable resin is often used for orientation in actual practice.[29,30] This three-dimensionally oriented microcrystal/resin composite is called magnetically oriented microcrystal array (MOMA). It shows the same diffraction image as a single crystal in actual measurements (Figure 7).[29,30] There are reports of successful X-ray crystal structure analysis using MOMA on inorganic crystal (cobalt lithium phosphate[30]), organic crystal (sucrose[32]), and protein crystal (lysozyme[33]). In addition, a combination of techniques using magnetic

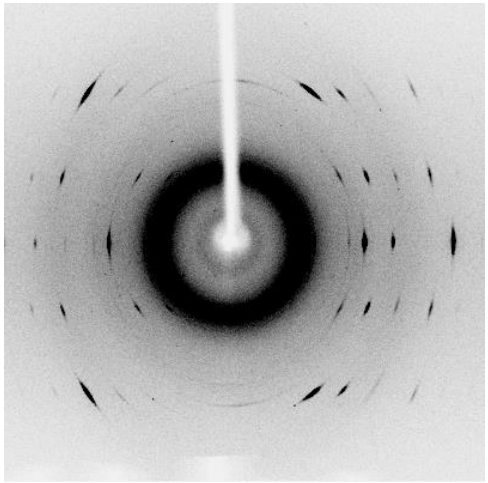

Figure 7. X-ray diffraction images of a magnetically oriented microcrystal array of L-alanine. This pattern is nearly the same to that of a single crystal.

field orientation and UV-curable resin is called the MOMA method. The MOMA method allows for single-crystal structure analysis from powder, but it has various problems that will be discussed below.

3. MOMA Method and Its Problems

The MOMA method has the following four drawbacks.

(1) It cannot collect microcrystal samples.[34]

The suspended microcrystals cannot be collected once the UV-curable resin has hardened. If sample collection is difficult, a rare sample cannot be analyzed using the MOMA method. Methods using thermoplastic resin dispersant and casting with polymer have also been considered theoretically, but because thermal denaturation of protein often occurs with temperature changes, the effect described in (2) is often encountered, thus none of these methods are realistic.

(2) Distortion of microcrystal orientation due to hardening of the resin.[34]

UV-curable resin shrinks with hardening. This shrinkage becomes a large factor in disturbing the orientation of microcrystals. Compared to the case of other orientation fixation methods such as the casting method, the degree of shrinkage of the UV-curable resin is small. If there is no resin shrinkage, improvement of the orientation is feasible.

(3) Large limitations on the suspension medium.[34]

There are few options for suspending mediums because it is impossible to use resins other than UV-curable resins. The microcrystal sample should not be dissolved or aggregated in the UV-curable resins, but the resins satisfying these conditions are sometimes difficult to find.

(4) The appropriate applied magnetic field conditions for microcrystal orientation are

not known.

In the MOMA method, the process of magnetic orientation is important, but in actual practice, a quantitative correlation between the magnetic condition and microcrystal orientation is not understood. Thus, it is important to conduct a carpet-bombing experiment in order to create a good MOMA of a microcrystal sample.

4. Outline of This Thesis

One of the objectives of this study is to develop a MOMA method without hardening the resin. This method should be like that the magnetically orientated microcrystal is not fixated in the suspension medium and goes directly for *in-situ* XRD measurement. For this purpose we perform *in-situ* XRD measurement of a magnetically oriented microcrystal suspension (MOMS). Because there is no hardening process in the MOMS method, sample collection is simple. Moreover, there is no effect of orientation disturbance due to hardening of the resin. Furthermore, there are more options for the suspending medium. Thus, problems (1), (2), and (3) of the MOMA method are solved, and crystal structure analysis using magnetic field orientation becomes possible for many other substrates.

In order to develop the MOMS method, first, a device was designed and manufactured for simultaneous measurement of the applied rotating magnetic field and XRD in this study. This was followed by actual *in-situ* XRD measurement of magnetically oriented microcrystals in suspension to analyze their crystal structure.

One more objective of the present study is to better understand the orientation of microcrystals in a magnetic field. This can solve problem (4) of the MOMA method by determining the optimal applied magnetic field conditions for microcrystal

orientation. *In-situ* XRD measurement is also very effective for this investigation because magnetic field application and the resulting microcrystal orientation condition can be immediately confirmed. In this study, we mainly investigated microcrystal orientation in static and rotating magnetic fields. In addition, with these magnetic fields applied to the microcrystals *in-situ*, the optimal conditions for microcrystal 3D orientation and XRD measurement are established.

Furthermore, while a major part of this study deals with the use of XRD measurement, we also attempted the application of the MOMA and MOMS methods for neutron diffraction measurement. Because the position of hydrogen atoms in a crystal can be easily identified with neutrons,[35] which is difficult when using X-rays, this would be very useful for analyzing the positions of hydrogen atoms, which is often important in the structure analysis of enzymes.[36] However, compared to X-ray analysis, neutron crystal structure analysis requires a large (millimeter order) single crystal. However, because this drawback rarely occurs with the MOMA and MOMS methods, these methods would have good compatibility with neutron structure analysis. In the present study, neutron diffraction measurements of a MOMA were conducted, and the possibility of and problems related to crystal structure analysis were summarized. In addition, MOMS neutron diffraction measurements were conducted, and its possibility was suggested.

The summary of this study is presented in Figure 8.

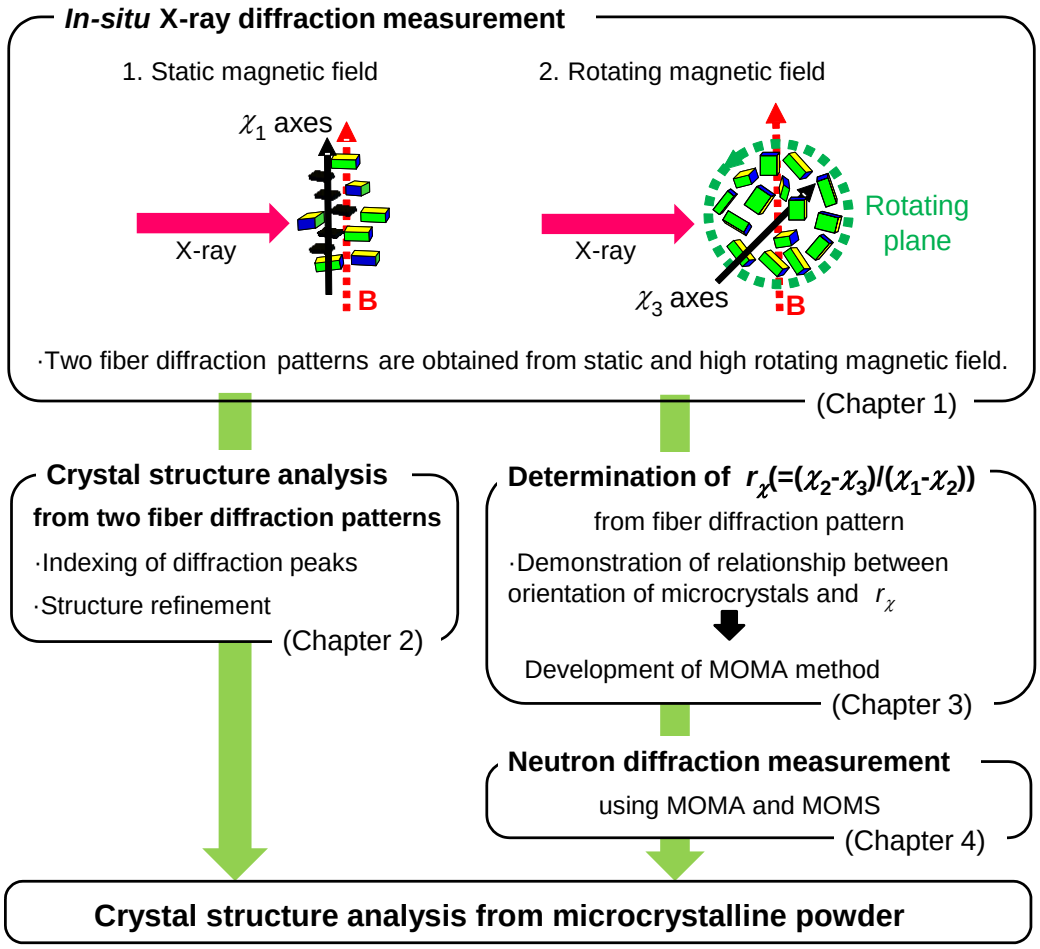

Figure 8. Schematic representation of the outline of this thesis.

Reference

[1] D. Mohan, C. U. Pittman Jr., P. H. Steele, *Energy & Fuels* **2006**, 20, 848.

[2] G. W. Huber, S. Iborra, A. Corma, *Chemical Reviews* **2006**, 106, 4044.

[3] H. K. Lonsdale, U. Merten, R. L. Riley, *Journal of Applied Polymer Science* **1965**, 9, 1341.

[4] D. Klemm, B. Heublein, H. P. Fink, A. Bohn, *Angewandte Chemie-International Edition* **2005**, 44, 3350.

[5] H. Yano, S. Nakahara, *J. Materials Science* **2004**, 39, 1635.

[6] S. B. Candanedo, M. Roman, D. G. Gray, *Biomacromolecules* **2005**, 6, 1048.

[7] M. E. Himmel, S. Y. Ding, D. K. Johnson, W. S. Adney, M. R. Nimlos, J. W. Brady, T. D. Foust, *Science* **2007**, 315, 804.

[8] M. N. Gupta, *Biotechnology and Applied Biochemistry*, **1991**, 1, 1.

[9] V. V. Mozhaev, *Trends in Biotechnology*, **1993**, 11, 3.

[10] T. Herrmann, P. Güntert, K. Wüthrich, *J. Mol. Biol.* **2002**, 319, 209.

[11] M. C. Sousa, C. B. Trame, H. Tsuruta, S. M. Wilbanks, V. S. Reddy, D. B. McKay, *Cell* **2000**, 103, 633.

[12] B. J. Graves, R. L. Crowther, C. Chandran, J. M. Rumberger, S. H. Li, K. S. Huang, D. H. Presky, P. C. Familletti, B. A. Wolitzky, D. K. Burns, *Nature* **1994**, 367, 532.

[13] J. C. Kendrew, G. Bodo, H. M. Dintzis, R. G. Parrish, H. Wyckoff, D. C. Phillips, *Nature* **1958**, 181, 662.

[14] C. C. Blake, D. F. Koenig, G. A. Mair, A. C. North, D. C. Phillips, V. R. Sarma, *Nature* **1965**, 206, 757.

[15] T. L. Blundell, L. N. Johnson, *Protein Crystallography*; Academic Press 1976

[16] M. Ataka, S. Tanaka, *Biopolymers* **1986**, 25, 337.

[17] K. D. M. Hariss, E. Y. Cheung, *Chem*. *Soc*. *Rev*. **2004**, 33, 526.

[18] I. Margiolaki, J. P. Wright, *Acta Crystallogr*. **2008**, A64, 169.

[19] T. Kimura, M. Yoshino, *Langmuir* **2005**, 21, 4805.

[20] T. Kimura, M. Yamato, W. Koshimizu, M. Koike, T. Kawai, *Langmuir* **2000**, 16, 858.

[21] T. Kimura, M. Yoshino, T. Yamane, M. Yamato, M. Tobita, *Langmuir* **2004**, 20, 5669.

[22] M. Yamaguchi, S. Ozawa, I. Yamamoto, *Jpn*. *J*. *Appl*. *Phys*. 2009, 48, 063001.

[23] G. Maret, K. Dransfeld, In *Topics in Applied Physics*; Herlash, F., Ed.; Springer-Verlag: Berlin, 1985; Vol. 57, Chapter 4.

[24] M. Fujiwara, T. Chidiwa, R. Tokunaga, Y. Tanimoto, *J*. *Phys*. *Chem*. *B* **1998**, 102, 3417.

[25] T. Kawai, R. Iijima, Y. Yamamoto, T. Kimura, *J*. *Phys*. *Chem*. *B* **2001**, 105, 8077.

[26] Y. Kaneko, T. Fukuda, T. Onodera, H. Kasai, S. Okada, H. Oikawa, H. Nakanishi, H. Matsuda, *Jpn*. *J*. *Appl*. *Phys*. **2003**, 42, L1343.

[27] T. Kimura, *Jpn*. *J*. *Appl*. *Phys*. **2009**, 48, 020217.

[28] M. Yamaguchi, S. Ozawa, I. Yamamoto, T. Kimura, *Jpn*. *J*. *Appl*. *Phys*. **2013**, 52, 013003.

[29] T. Kimura, F. Kimura, M. Yoshino, *Langmuir* **2006**, 22, 3464.

[30] T. Kimura, C. Chang, F. Kimura, M. Maeyama, *J*. *Appl*. *Crystallogr*. **2009**, 42, 535.

[31] M. Yamaki, S. Horii, M. Haruta, J. Shimoyama, *Jpn*. *J*. *Appl*. *Phys*. **2012**, 51, 010107.

[32] F. Kimura, T. Kimura, W. Oshima, M. Maeyama, K. Aburaya. *J*. *Appl*. *Crystallogr*. **2010**, 43, 151.

[33] F. Kimura, K. Mizutani, B. Mikami, T. Kimura, *Cryst*. *Growth Des*. **2011**, 11, 12.

[34] K. Matsumoto, F. Kimura, S. Tsukui, T. Kimura, *Cryst*. *Growth Des*. **2011**, 11, 945.

[35] A. T. Brünger, M. Karplus, *Proteins* **1988**, 4, 148.

[36] N. Niimura, *Curr*. *Opin*. *Struct*. *Biol*. **1999**, 9, 602.

Chapter 1. *In-Situ* XRD Measurement of Magnetically Oriented Microcrystal Suspension

1.1 Introduction

MOMS method is a method of crystal structure analysis involving *in-situ* XRD measurement of magnetically oriented microcrystals in a suspension. As explained in Section 2 of the General Introduction, because the magnetic orientation is performed mainly by a rotation of magnetic field, it is of primary importance to develop a device that applies a rotating magnetic field to the sample. Then, in order to obtain a good *in-situ* XRD image, it is important to understand the correlation between the magnetic field to be applied and the magnetic properties of the microcrystal under consideration. Recently, there have been studies on the correlation between the magnetic field to be applied and the microcrystal orientation, but those studies have assumed an infinite rotation speed (rapid rotation regime (RRR)).[1-3] However, because infinite rotation speed is impossible to achieve, actual experiments have been performed under a finite rotation speed.[4,5] In this condition, the orientation behavior may be different from that under an infinite rotation. However, the effect of slow rotation is not yet clearly understood especially for rotation speeds under these regimes including synchronous rotation regime (SRR) and asynchronous rotation regime (ARR)).

Thus, in this section, the correlation between the rotation speed and microcrystal orientation is investigated using simulations and *in-situ* XRD measurements. In addition, based on this evaluation, the optimum condition is determined and *in-situ* XRD measurement is conducted under those conditions. L-Alanine microcrystals are used as the samples.

1.2 Material and Methods

1.2.1 Preparation of Rotating System

We built a rotating unit (KU model χ10-1) that can rotate a microcrystalline suspension under various rotation types in a static magnetic field. Figure 1.1 shows a photograph of the rotating unit. The magnetic field is generated by a magnetic circuit formed by two magnets facing each other. Both magnets are spherical with a diameter of 3.0 cm. Magnetic flux density can be adjusted from 1.26, 1.07 to 0.81 T by changing the distance between the two magnets. A capillary tube containing a microcrystalline suspension was rotated in this magnetic field. A stepping motor (103F3505-744, Melec) was employed to rotate the capillary tube. This motor is operated by a controller (C772) and a driver (GDB-5F30) and is capable of variations such as modulated rotation in addition to constant rotation. To prevent axial vibration, a shaft and a cap ring are placed between the motor and the capillary tube.

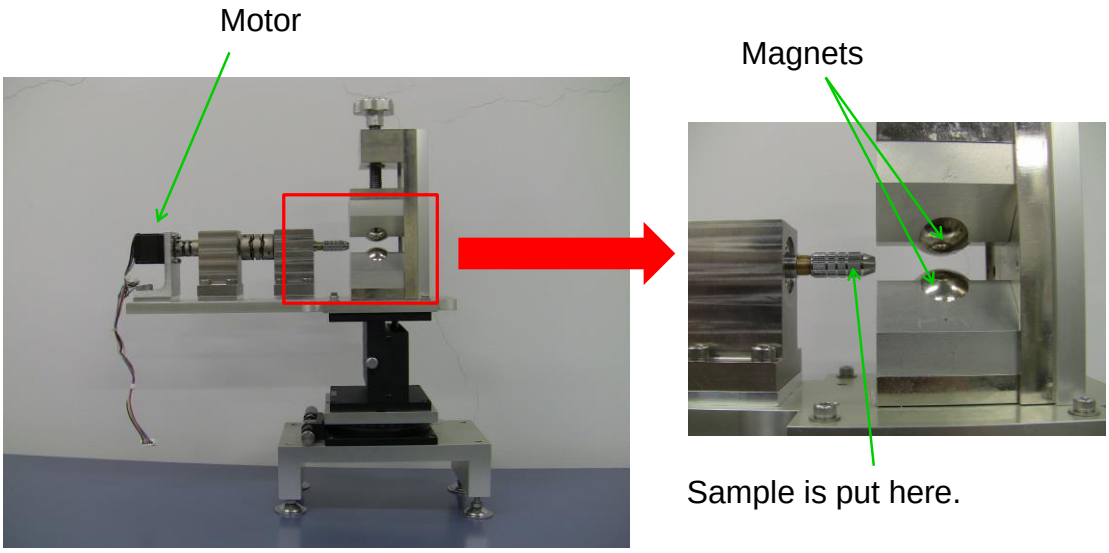

Figure 1.1. Photograph of a rotating unit (KU model χ10-1). The suspension of a sample is rotated in a static magnetic field and subjected to *in-situ* X-ray diffraction measurement.

1.2.2 Preparation of Microcrystalline Suspension

An as-received sample of L-alanine (Wako) crystals was pulverized using a mortar and pestle to pass 125-, 75-, and 20-mesh sieves consecutively, and the powder remaining on the 20-mesh sieve was used. The obtained powder (0.20 g) was suspended in 1 mL of polyethylene glycol (PEG#300) to prepare a suspension, which was then poured into a glass capillary (2 mm in diameter).

1.2.3 *In-Situ* X-ray Diffraction Measurement

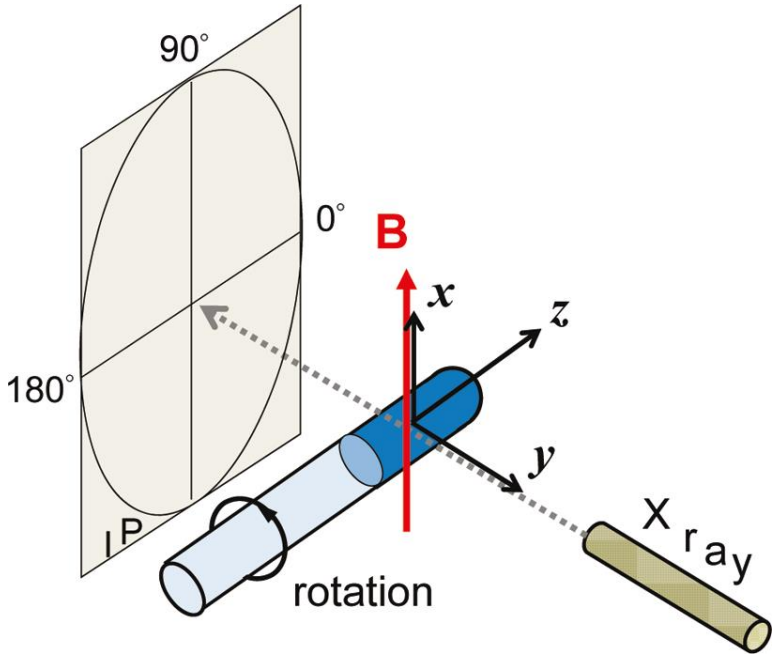

Figure 1.2. Experimental setting of *in-situ* X-ray diffraction measurement of a microcrystal suspension. A glass capillary containing the suspension is rotated at the rotation speed ω about the *z*-axis. The magnetic field **B** is applied parallel to the *x*-axis. The X-ray beam is impinged from the *y* direction, and the diffractions are detected by an imaging plate (IP). The azimuthal β angle is indicated.

The capillary containing the suspension was placed on a rotating unit (KU model χ10-1) equipped with a pair of sphere-type neodymium magnets (3 cm in

diameter, producing ca. 1 T in the center). The experimental setting is schematically shown in Figure 1.2. Then, the rotating unit was placed in a MAC Science Dip 2000 diffractometer equipped with an MXP18HF22 rotating anode generator (45 kV, 84 mA). Graphite-monochromated Cu Kα radiation was used. The collimator size was 0.9 mmϕ. The rotation speeds ω were chosen between 0 (static) and 20 rpm. During a 30-min duration of rotation at a given rotation speed, six 5-min X-ray measurements were performed. The azimuthal β-scan for a given 2θ diffraction was baseline-corrected by subtracting the intensity in the vicinity of the respective 2θ.

1.2.4 Simulating Orientation Behavior of Microcrystals in Rotating Magnetic Field

Using Mathematica, we simulated the orientation behavior of L-alanine crystals in suspension in a rotating magnetic field. A magnetic torque $\mathbf{T}_m$ and a hydrodynamic torque $\mathbf{T}_h$ were applied to biaxial crystals in the suspension in a rotating magnetic field. Ignoring the inertial terms, which are negligible because of small crystal size and high viscosity, the following equation of motion is obtained:

$$\mathbf{T}_m+\mathbf{T}_h=0, \tag{1.1}$$

where the magnetic torque $\mathbf{T}_m$ is given as follows:

$$\mathbf{T}_m=V({}^t\mathbf{A}\chi\mathbf{A}\cdot\mathbf{H})\times\mu_0\mathbf{H}, \tag{1.2}$$

where V is the volume of the crystals, $\mathbf{A}$ is a coordinate transformation matrix using Euler angles, χ is the magnetic susceptibility tensor, $\mathbf{H}$ is the magnetic field intensity,

and μ_0 is the magnetic permeability of vacuum. The hydrodynamic torque $\mathbf{T}_h$ is given as follows:

$$\mathbf{T}_h = -\eta\,({}^t\mathbf{ALA})\cdot\mathbf{\Omega}, \tag{1.3}$$

where η is the viscosity of the suspension, **L** is a hydrodynamic tensor, and **Ω** is the angular velocity.

As we could not solve the eq. (1.1) analytically, we performed a numerical calculation. The laboratory coordinate system, *xyz*, and the magnetization coordinate system, $\chi_1\chi_2\chi_3$, are transformed by the Euler angles (ϕ, θ, ψ) (Figure 1.3). Here the rotating magnetic field was applied on the *xy* plane. Assuming a spherical shape for microcrystals, we performed numerical calculations for ten different initial orientations. As we assumed the orientation in a static magnetic field as the initial state, we chose the initial conditions such that the χ_1 axis is oriented along the *x* axis and the χ_3 axis has the following different orientations: 0^o, 10^o, 20^o, 30^o, 40^o, 50^o, 60^o, 70^o, 80^o, 90^o.

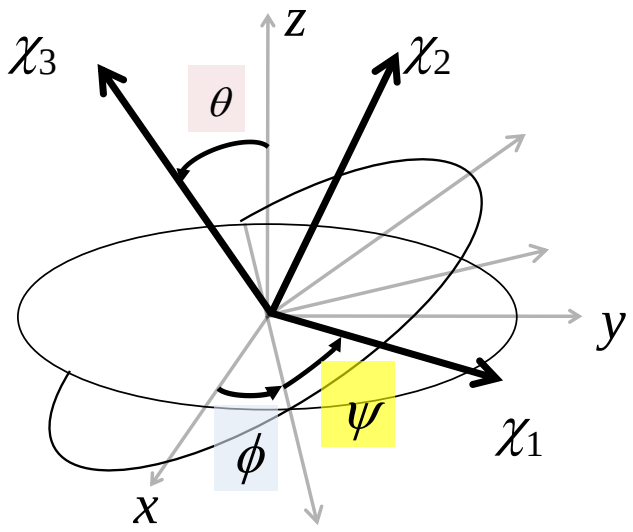

Figure 1.3. The magnetic susceptibility axes referred to the laboratory *xyz* coordinates through Euler angles Magnetic field rotates in the *xy*-plane.

1.3 Results and Discussion

1.3.1 Rotation Speed Dependence of Microcrystal Orientation

The relationship between the magnetization axes and crystallographic axes of L-alanine (orthorhombic, $P2_12_12_1$, a = 6.032, b = 12.343, c = 5.784 Å) is known to be $\chi_1 \| c^*$, $\chi_2 \| a^*$, and $\chi_3 \| b^*$[6,7] as shown in Figure 1.4. When the suspension is not rotated, the reciprocal c^* axis aligns parallel to the magnetic field ($\| x$), while the reciprocal a^* and b^* axes are distributed uniformly on the yz plane (Figure 1.4). On the other hand, when the suspension is rotated about the z-axis at a sufficiently rapid speed (ARR or RRR),[8] the b^* axis aligns parallel to the z-axis, while the a^* and c^* axes are located on the xy plane, rotating with the rotation of the medium.

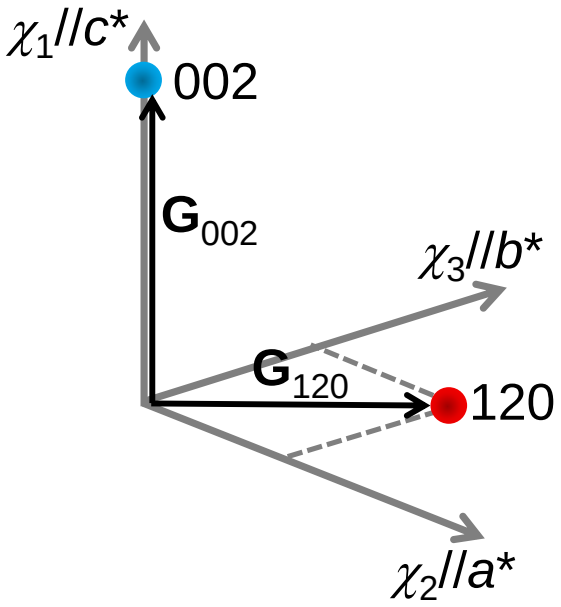

Figure 1.4. Relationship between the magnetic axes χ_1, χ_2, and χ_3 and the crystallographic reciprocal axes a^*, b^*, and c^* in the reciprocal space. Since L-alanine is orthorhombic, the magnetic axes and crystallographic axes are parallel to each other. The reciprocal vectors $\mathbf{G}_{002}$ and $\mathbf{G}_{120}$, indicating the (002) and (120) planes, respectively, are also shown.

Figure 1.5 shows the 18 diffraction patterns obtained for ω = 0 rpm (static) to 20 rpm. At ω = 0 rpm, the {002} diffractions did not appear, and the {120} diffractions appeared on the equator. This suggests that the reciprocal vectors $\mathbf{G}_{\{002\}}$ are aligned in the direction of the applied magnetic field ($\|x$) and the reciprocal vectors $\mathbf{G}_{\{120\}}$ are distributed randomly on the *yz* plane. Because the crystal has three mutually orthogonal 2-fold axes (*a*, *b*, and *c* axes), the diffractions belonging to {120} are not distinguishable in a MOMA, neither are the diffractions (002) and (002). With an increase in rotation speed, the {120} diffractions on the equator disappeared and moved to locations around 45°, 135°, 225°, and 315°. On the other hand, the {002} diffractions appeared in the southern hemisphere on the meridian at rotation speed 0.3~1.2 rpm. These indicate that the *b** axis was directed to the *z*-axis and the *c** axis and the *a** axis rotated on *xy* plane at rotation speed 1.5~20 rpm. The alignment of the χ_3 axis ($\|b^*$) in the direction of the rotation axis ($\|z$) is expected based on the behavior of a magnetically uniaxial particle.[2,8]

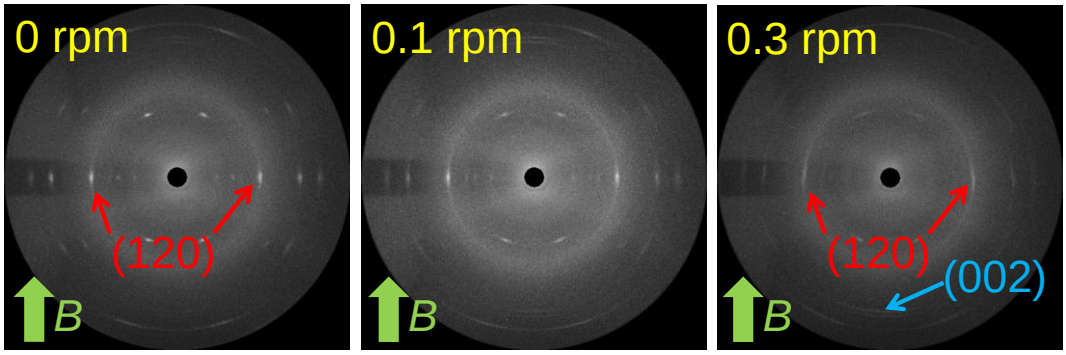

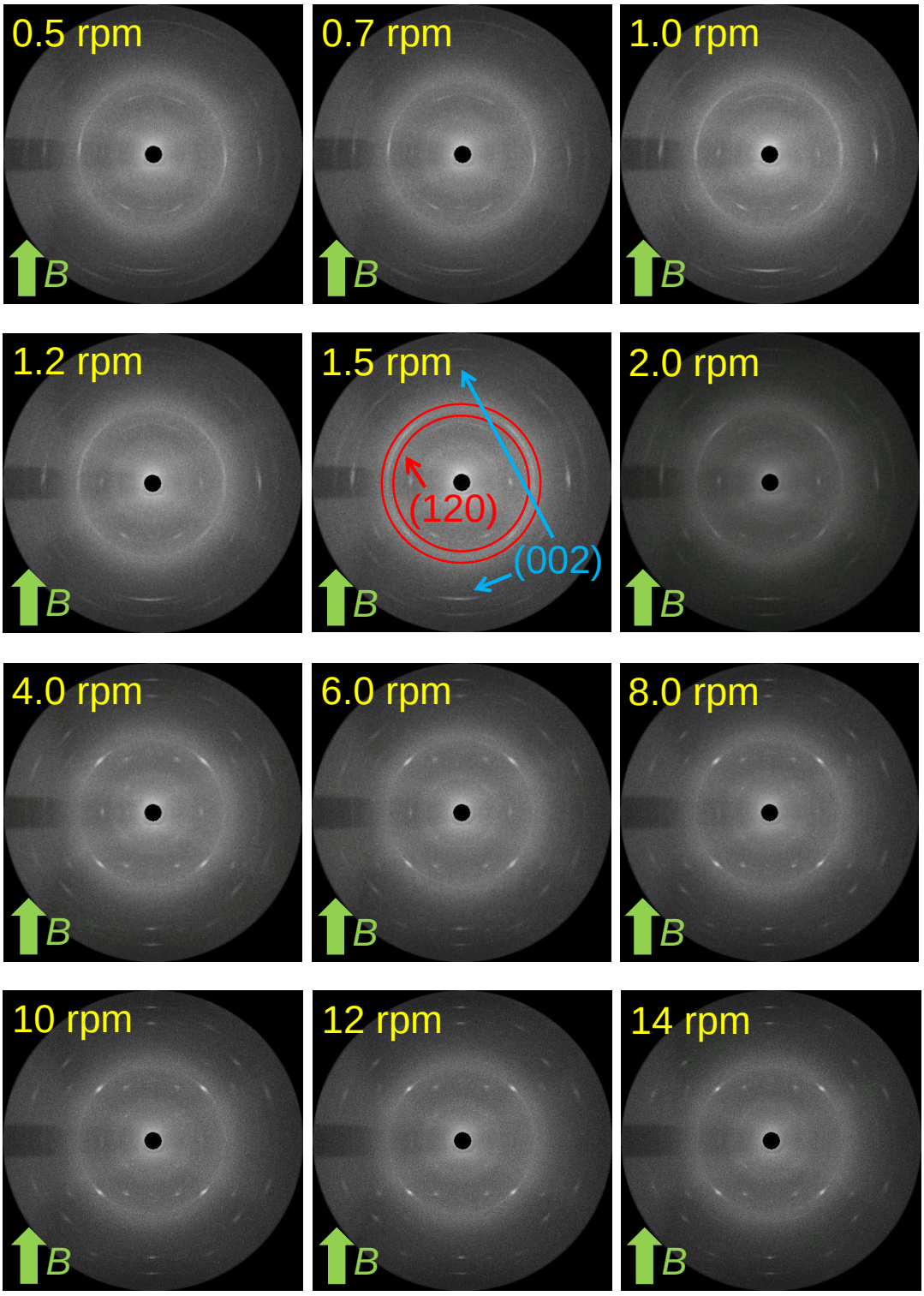
0.5 rpm
0.7 rpm
1.0 rpm
1.2 rpm
1.5 rpm
(120)
(002)
2.0 rpm
4.0 rpm
6.0 rpm
8.0 rpm
10 rpm
12 rpm
14 rpm
B

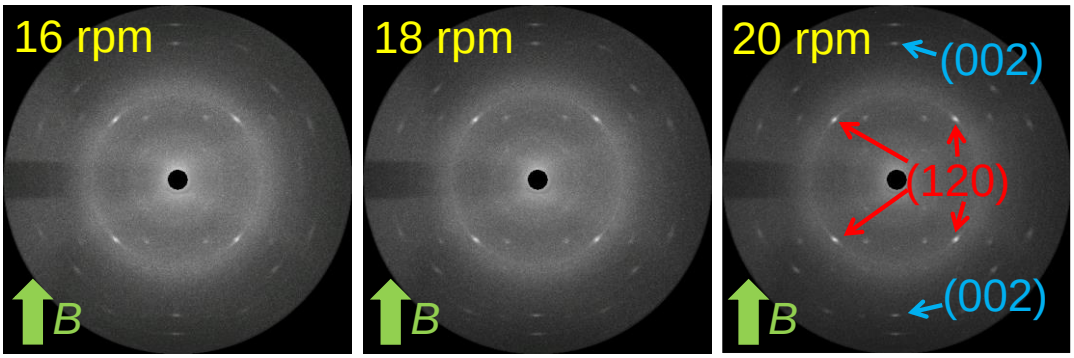

Figure 1.5. X-ray diffraction images of a magnetically oriented microcrystal suspension (MOMS) obtained at ω = 0, 0.1, 0.3, 0.5, 0.7, 1.0, 1.2, 1.5, 2.0, 4.0, 6.0, 8.0, 10, 12, 14, 16, 18 and 20 rpm. The locations of {002} and {120} planes are shown in the diffraction patterns 0, 0.3, 1.5, and 20 rpm.

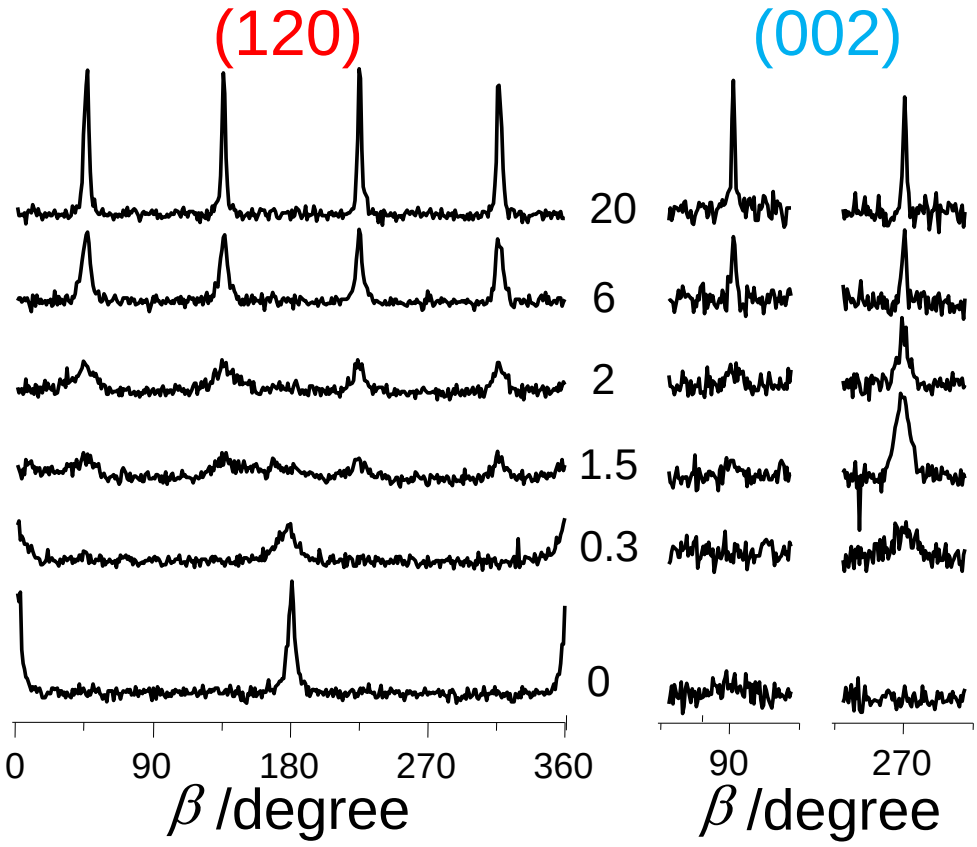

Figure 1.6. Azimuthal plots of the {120} and {002} diffractions for various values of rotation speed ω.

Figure 1.6 shows the azimuthal β -scan for the {120} and {002} planes, respectively, for various values of ω. As observed in Figure 1.5, the {120} diffractions were observed at β = 0 and 180^{o} (corresponding to the equator), and the {002} diffractions were not observed at ω=0 rpm. With an increase in ω, the {120} diffractions on the equator became weak and finally disappeared at ω = 1.5-2 rpm, and new diffraction spots started to appear around 45^{o}, 135^{o}, 225^{o}, and 315^{o}. On the other hand, the {002} diffraction (β = 270^{o}) started to appear at ω = ca. 0.3 rpm in the southern hemisphere. At ω = 6 rpm, the {002} diffraction (β = 90^{o}) also appeared in the northern hemisphere.

These observations are interpreted as follows: At ω = 0 rpm (static field), the χ_1 axis (||*c**) aligned parallel to the *x*-axis, and the other magnetic axes were distributed on the *yz* plane. Then, the $\mathbf{G}_{\{002\}}$ did not cross the Ewald sphere, whereas the $G_{\{120\}}$ did (Figure 1.7a). At ω = 0.3~1.2 rpm, the χ_1 axis could no longer remain parallel to the *x*-axis and inclined with respect to the *x* axis, resulting in the contact of $\mathbf{G}_{\{002\}}$ with the Ewald sphere in the southern hemisphere. The χ_3 axis (||*b**) were distributed randomly around the χ_1 axis (Figure 1.7b). At ω = 2.0 rpm, the χ_3 axis (||*b**) started to align toward the *z*-axis, driving the $\mathbf{G}_{\{120\}}$ away from contact with the Ewald sphere, resulting in a decrease in {120} intensity. Upon further increase in the rotation speed (ω = 2-20 rpm), the χ_1 axis (||*c**) could no longer stay inclined with respect to the *x*-axis, and it rotated about the *z*-axis, with the χ_3 axis (||*b**) remaining aligned with the *z*-axis. As a result, the $\mathbf{G}_{\{120\}}$ and $\mathbf{G}_{\{002\}}$ crossed the Ewald sphere, giving rise to four spots for {120} and two spots for {002}, respectively (Figure 1.7c). This state is termed ARR. Moreover, Figure 1.6 indicates that at a rotation speed of 1.5 rpm there are six {120} diffraction peaks: β = 0^{o},45^{o}, 135^{o}, 180^{o}, 225^{o}, and 315^{o}. This suggests that diffraction

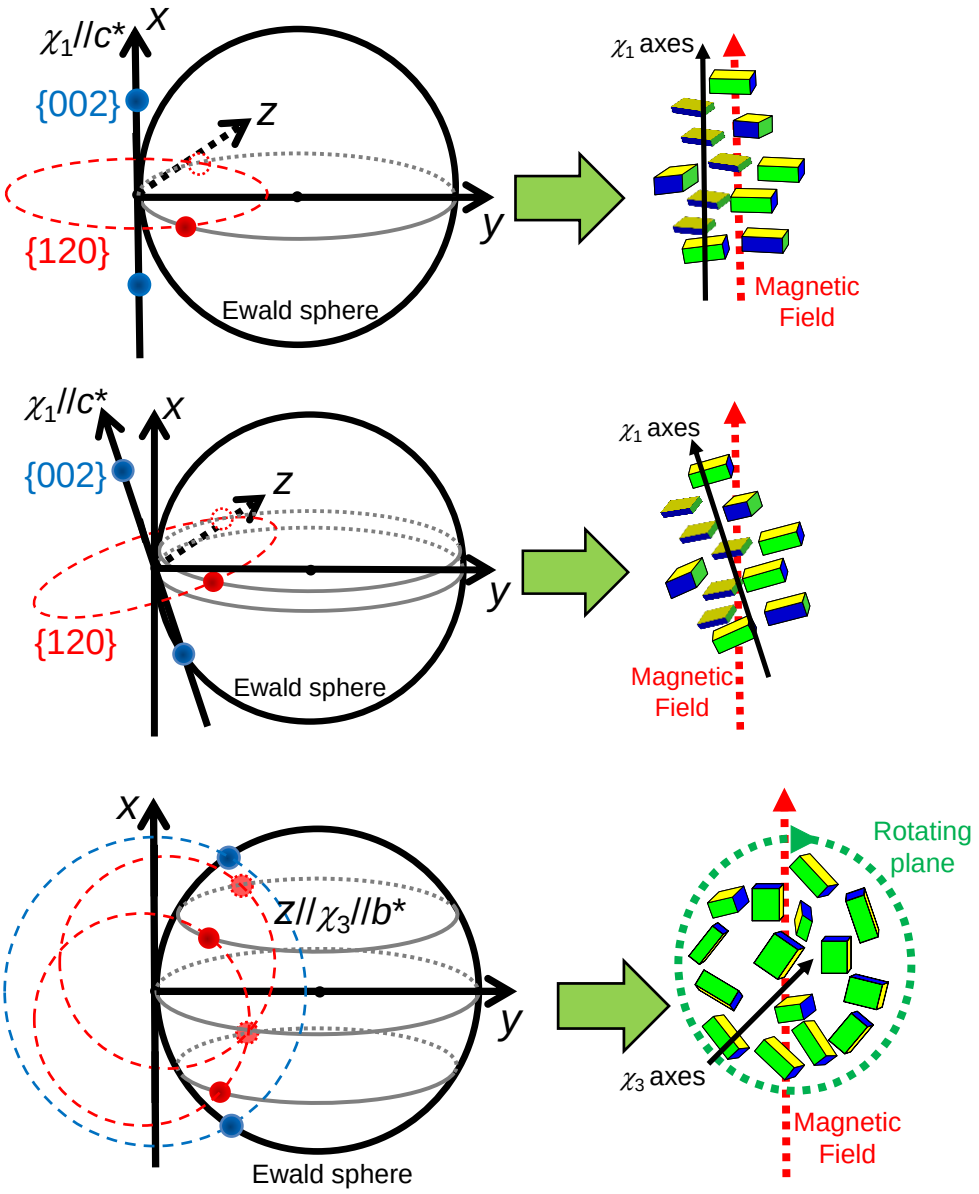

Figure 1.7. Schematic diagrams to explain the diffraction patterns obtained at $\omega = 0$, 0.3, and 20 rpm. (a) At $\omega = 0$ rpm, the easy magnetization axis ($\chi_1 \| c^*$) aligns in the *x*-direction, and $\chi_2 \| a^*$ and $\chi_3 \| b^*$ are randomly distributed on the *yz* plane, giving rise to the {120} diffraction on the equator. (b) At $\omega = 0.3$ rpm, the χ_1 axis incline with respect to the *x*-direction, and $\chi_2 \| a^*$ and $\chi_3 \| b^*$ are randomly distributed on the perpendicular plane to χ_1 axis. (c) On the other hand, at $\omega = 20$ rpm the hard magnetization axis ($\chi_3 \| b^*$) aligns parallel to the rotating axis (the *z*-axis), and $\chi_2 \| a^*$ and $\chi_1 \| c^*$ are rotating on the *xy* plane, resulting in four diffraction spots of the {120} and two diffraction spots of {002}.

peaks due to microcrystals in the SRR state and those due to microcrystals in the ARR state were both observed. That is, there is a condition in which microcrystals in the SRR state and those in the ARR state coexist.

1.3.2 Comparison between Experiment and Simulation

Figure 1.8 shows the temporal change of the Euler angles (ϕ, θ, ψ) at rotation speeds of 0.3, 1, 2, 3, 4, 6, 8, 16, 20, and 30 rpm. At rotation speeds of 0.3, 1, and 2 rpm, the value of ϕ coincided with the angle ωt between the magnetic field and the *x* axis, and the value of θ remained near the initial value. The value of ψ nearly converged to a constant after a sufficiently long period, and this value was greater for higher rotation speeds. If ϕ is ωt and ψ converges to a constant, it indicates that the χ_1 axis and the magnetic field form a constant angle in the *xy* plane. Moreover, if the value of θ remains close to the initial value, the χ_2 and χ_3 axes are randomly oriented perpendicular to the χ_1 axis. This state corresponds to the SRR state shown in Figure 1.7b. Furthermore, if $\phi = \omega t$ and the absolute value of ψ increases with increasing rotation speed, it indicates that the angle between the χ_1 axis and the magnetic field increases with increasing rotation speed. Figure 1.5 shows that in a range from 0 rpm to 1.0 rpm, the intensity of the (002) diffraction peaks that appeared in the southern hemisphere increased with increasing rotation speed. That is, as the rotation speed increases from 0.1, 0.3 to 0.5, the angle between the χ_1 axis and the magnetic field increases, and the reciprocal lattice point 002 approaches the Ewald sphere in the southern hemisphere, resulting in increased intensity of the (002) diffraction peaks in the southern hemisphere with increasing rotation speed.

However, for rotation speeds of 6 rpm or higher in Figure 1.8, the value of ϕ

becomes smaller than ωt and the value of θ converges to 0. The value of ψ fluctuates around 0 and its amplitude decreases with increasing speed. We discuss the crystal orientations based on the above observation. As the value of ϕ is smaller than ωt, the angle between the χ_1 axis of the crystal and the magnetic field is not constant in the ARR state. The value of θ converges to 0, indicating that the χ_3 axis is oriented in the direction of the rotation axis. This is the ARR state shown in Figure 1.7c. The value of ψ fluctuating around 0° and the value of θ near 0 indicate that the χ_1 axis rotates and vibrates on the rotation plane. However, this is not the case for the *in-situ* X-ray diffraction pattern.

In Figure 1.8, the value of ϕ is equal to ωt at 3 and 4 rpm, as similarly observed at 0.3–2 rpm. Depending on the initial value, the value of θ for the crystals either remained at the initial value or converged to 0. For the crystals whose θ remained at the initial value, the value of ψ remained at 0; however, for the crystals whose θ converged to 0, the value of ψ diverged to negative infinity. This corresponds to the experimental results for ω=1.5 rpm. The crystals whose ψ diverged were those whose θ converged to 0. When the value of θ converges to 0, the χ_1 axis is on the rotation plane, and therefore, the position of the χ_1 axis on the rotation plane can be described as $\phi - \omega t + \psi$. If this value is constant, the angle between the χ_1 axis and the magnetic field is constant. However, as the value of ψ diverges to negative infinity, the angle $\phi - \omega \tau + \psi$ does not become a constant value, and the χ_1 axis and the magnetic field is not separated by a constant angle. In other words, the crystals whose ψ is almost constant exhibit SRR behavior, and the crystals whose ψ diverges to negative infinity exhibit ARR behavior. Therefore, the simulation also indicates that crystals exhibiting SRR and ARR behaviors coexist under these speed

conditions. Furthermore, the simulation revealed that the initial position is the main factor.

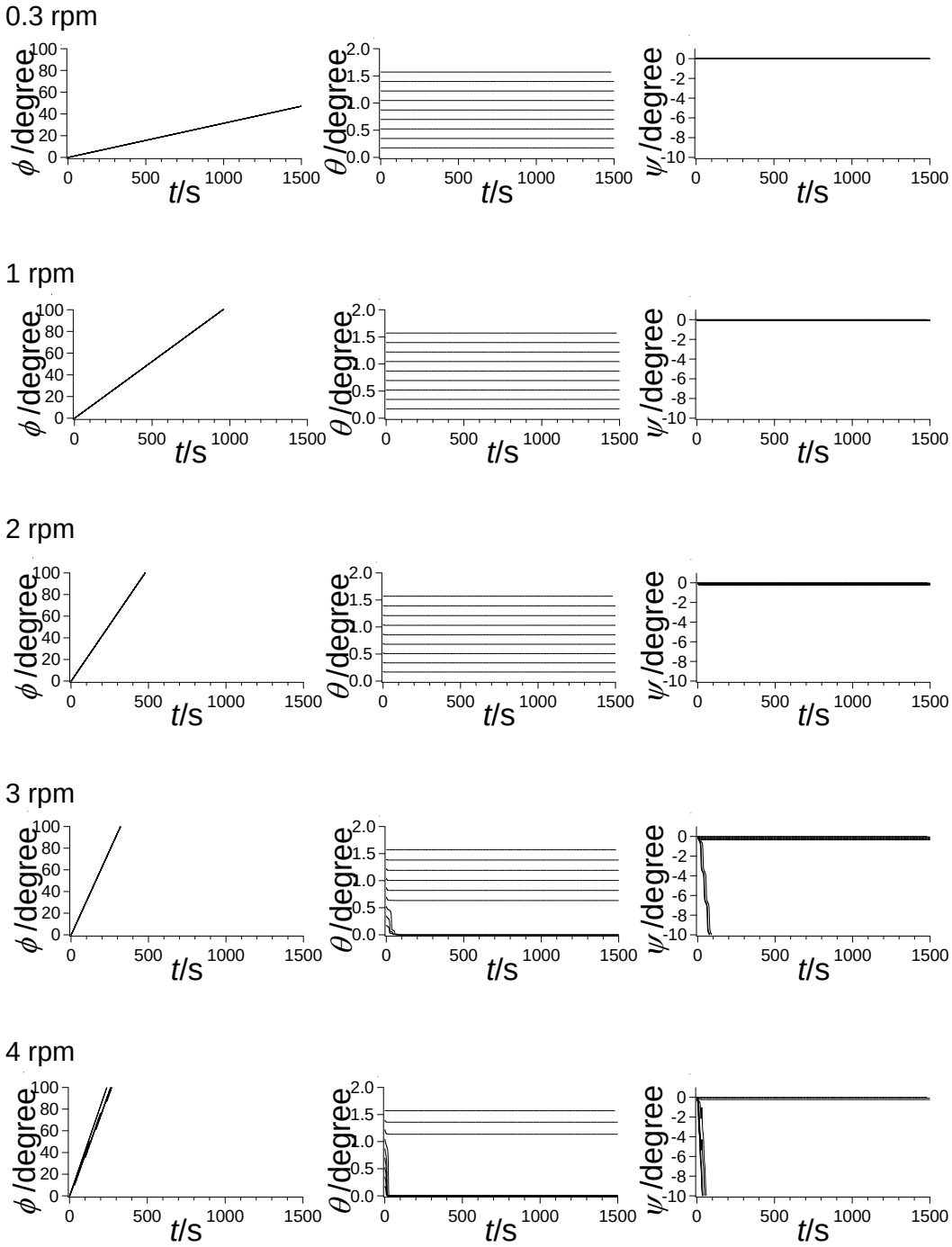

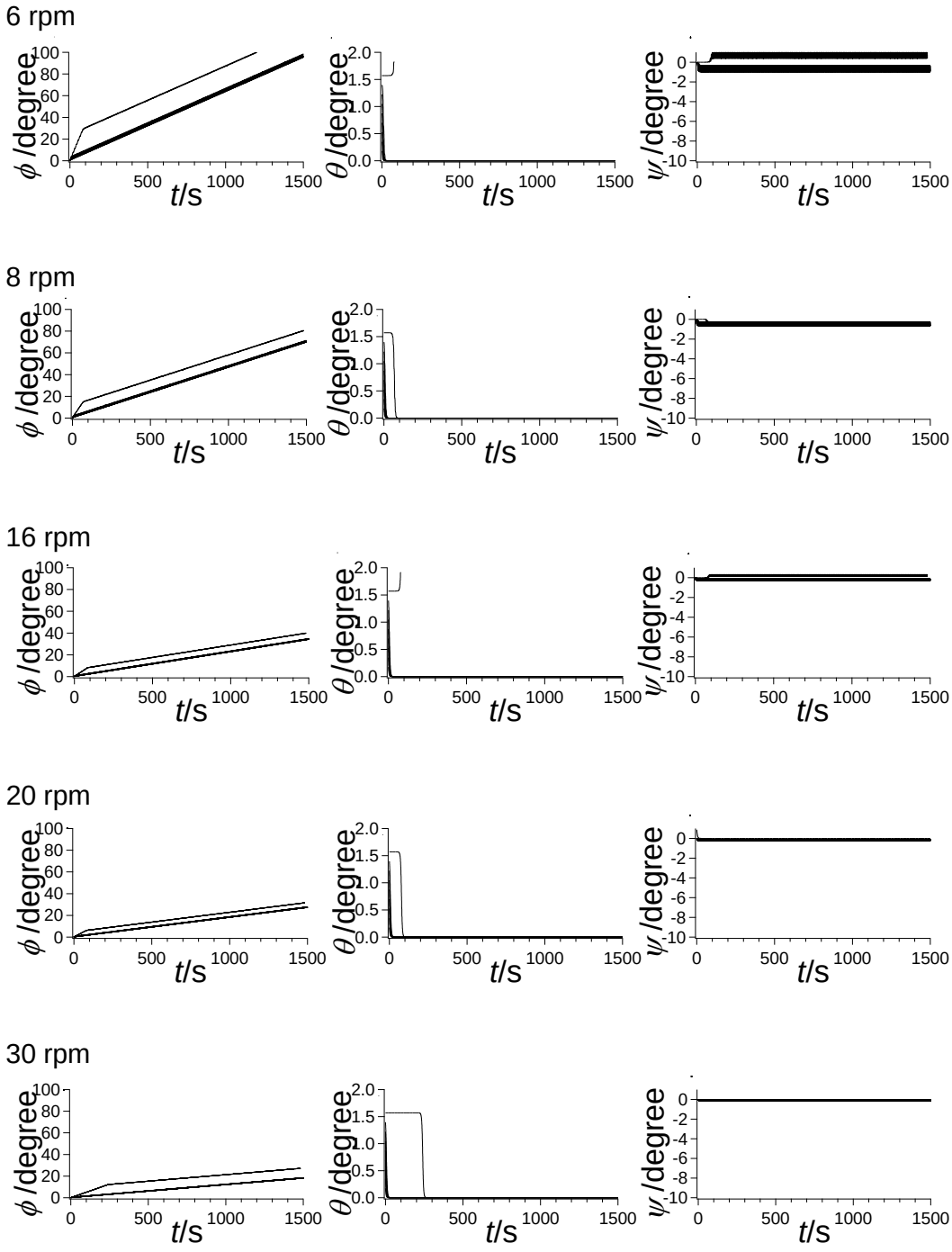

Figure 1.8. The Euler angles plotted as a function of time for various rotation speeds.

1.3.3 Tuning of Experimental Condition to Obtain High Degree of Orientation

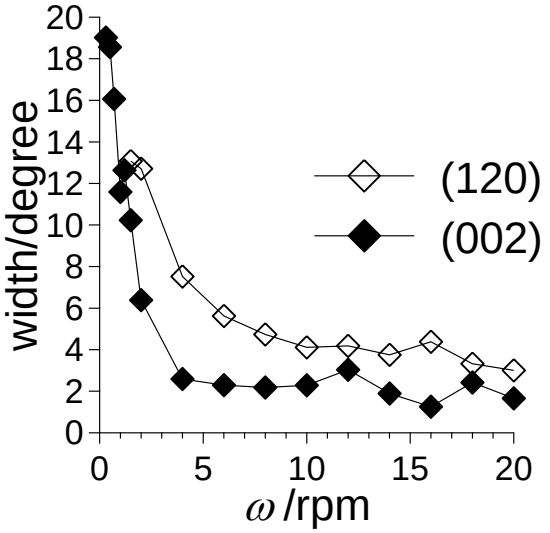

Figure 1.9. Half widths of the diffraction spots of {120} and {002} plotted against rotation speed ω.

In Figure 1.9, the half widths of the {120} and {002} diffraction spots are plotted as a function of the rotation speed ω. Faster rotation resulted in sharper diffraction spots. In the limit of the RRR, the half width is independent of ω, reaching a constant value as described below. The half width is related to the thermal fluctuation of the magnetic axes in a potential well produced by the magnetic field.[1] Truncating the higher terms, we can express the magnetic energy in the vicinity of the minimum as

$$E_{\mathrm{S}} = \frac{(\chi_1 - \chi_2 \cos^2 \Phi_{\mathrm{S}} - \chi_3 \sin^2 \Phi_{\mathrm{S}}) V B^2 \sin^2 \alpha_{\mathrm{S}}}{2\mu_0}$$
$$E_{\mathrm{R}} = \frac{(\chi_1 \cos^2 \Phi_{\mathrm{R}} + \chi_2 \sin^2 \Phi_{\mathrm{R}} - \chi_3) V B^2 \sin^2 \alpha_{\mathrm{R}}}{4\mu_0},$$

(1.4)

where the subscripts S and R indicate "static" and "rotating," respectively, μ_0 is the magnetic permeability of vacuum, V is the volume of a crystal, and B is the magnetic flux density.[9] α_S is the angle between χ_1 and the static field, and α_R is the angle between χ_3 and the rotation axis. The angle Φ_S is shown in Figure 1.10a, and the angle Φ_R is shown in Figure 1.10b. By averaging using the Boltzmann factor, we obtain the following fluctuations:

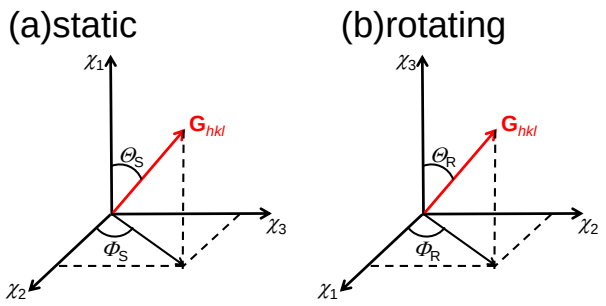

Figure 1.10. The angles Θ and Φ that characterize the direction of the reciprocal lattice vector **G** with respect to the $\chi_1\chi_2\chi_3$ coordinates in the case of (a) a static magnetic alignment and (b) a rotating magnetic alignment.

$$\langle \alpha_S^2 \rangle = \frac{k_B T \mu_0}{VB^2}\left\{\frac{1}{\chi_1-\chi_2} - \frac{(\chi_2-\chi_3)\sin^2\Phi_S}{(\chi_1-\chi_3)(\chi_1-\chi_2)}\right\}$$
$$\langle \alpha_R^2 \rangle = \frac{2k_B T \mu_0}{VB^2}\left\{\frac{1}{\chi_1-\chi_3} - \frac{(\chi_1-\chi_2)\sin^2\Phi_R}{(\chi_1-\chi_3)(\chi_2-\chi_3)}\right\},$$

(1.5)

where k_B and T are the Boltzmann constant and temperature, respectively. The fluctuations obtained above are related to the half width (Hi (i=S or R)) of (hkl) plane:[10]

$$H_S^2 = \frac{Cf_S^2}{2}\left\{\frac{1}{\chi_1-\chi_2} - \frac{(\chi_2-\chi_3)\sin^2\Phi_S}{(\chi_1-\chi_3)(\chi_1-\chi_2)}\right\}$$
$$H_R^2 = Cf_R^2\left\{\frac{1}{\chi_1-\chi_3} + \frac{(\chi_1-\chi_2)\sin^2\Phi_R}{(\chi_1-\chi_3)(\chi_2-\chi_3)}\right\},$$

(1.6)

where $C=2k_BT\mu_0(VB^2)^{-1}$ and *fi* is a geometrical correction and is obtained by the following equation:

$$f_i^2 = \frac{4A^2 \sin^2 \Theta_i}{4A^2 \sin^2 \Theta_i - G^2}. \quad (1.7)$$

Here, Θi is the angle characterizing the direction of the reciprocal vector **G**(*hkl*) relative to the $\chi_1\chi_2\chi_3$ frame as shown in Figure 1.10, *G* is the length of the reciprocal vector **G**(*hkl*), and *A* is the wave number of the X-ray.

We use the following parameters: B =1.06 T, χ_1=-9.8×10^{-6}, χ_2=-10.1×10^{-6}, χ_3=-10.4×10^{-6},[7] and T = 300 K. Since the size distribution is unknown, we assumed average values for the volume and estimate the values of the half width. For V = (20×10^{-6})^3 m^3 (20 μm in linear size), we obtain H_R=0.08^o and 0.12^o for the (002) and (120) planes, respectively. On the other hand, for V = (2×10^{-6})^3 m^3 (2 μm in linear size), we obtain H_R=2.61^o and 3.67^o for the (002) and (120) planes, respectively. The latter values are close to the experimentally observed half widths. Although the 20-mesh sieve was used, many microcrystals smaller than 2 μm were observed in the suspension under a microscope. Therefore, 2 μm may not be far from the actual average size of the microcrystals in the suspension used in this study. We therefore conclude that the theoretical half width can be achieved if we use a suspension. In the case of MOMA, where the orientation is consolidated, we generally have to use 8 T or more in order to obtain the half width of the same level as that obtained for MOMS. This is probably because the achieved orientation is partially randomized in MOMA by the consolidation process.[4,11,12]

The conditions necessary to achieve high resolution are summarized as follows. (i) The individual microcrystals should not be polycrystalline, but they should be single crystals. (ii) The concentration of the microcrystal should usually be 10-20%. If it is too dilute, the diffraction intensity is insufficient, and if it is too concentrated, a perfect alignment may not be achieved because the alignments interfere with each other. (iii) The density of the suspending medium should be as close as possible to that of the crystal to prevent sedimentation or floatation of microcrystals. (iv) The rotation speed should be set high enough to achieve sufficiently narrow half widths. However, with increase in rotation speed, the centrifugal force becomes effective, deteriorating the alignment. This effect is large when the mismatch between the densities of the suspending medium and the particle is large.

1.4 Summary

To conclude, we successfully obtained two fiber X-ray diffraction patterns from *in-situ* X-ray diffraction measurement with and without rotation of the microcrystal suspension (crystal size of ca. 2-20 μm) in a magnetic field (1 T). Diffraction spots were sharp (ca. 2-3^{o} in half width) and well separated. The present results suggest a potential use of MOMS for crystal structure analysis of solid materials that do not grow into large crystals but are obtained in the form of microcrystal suspensions.

Furthermore, we discovered the following facts about orientation of biaxial crystals in a rotating magnetic field. With a small rotation speed (SRR), the χ_1 axis of the microcrystal follows the rotation and remains near the magnetic field. In this case, the χ_2 and χ_3 axes are not oriented. As the rotation speed increases (ARR), the χ_1 axis

of the microcrystal cannot follow the rotation of the magnetic field. On the other hand, the χ_3 axis is oriented in the direction of the rotation axis. The degree of orientation of the χ_3 axis depends on the rotation speed. Figure 1.11 summarizes the above statements.

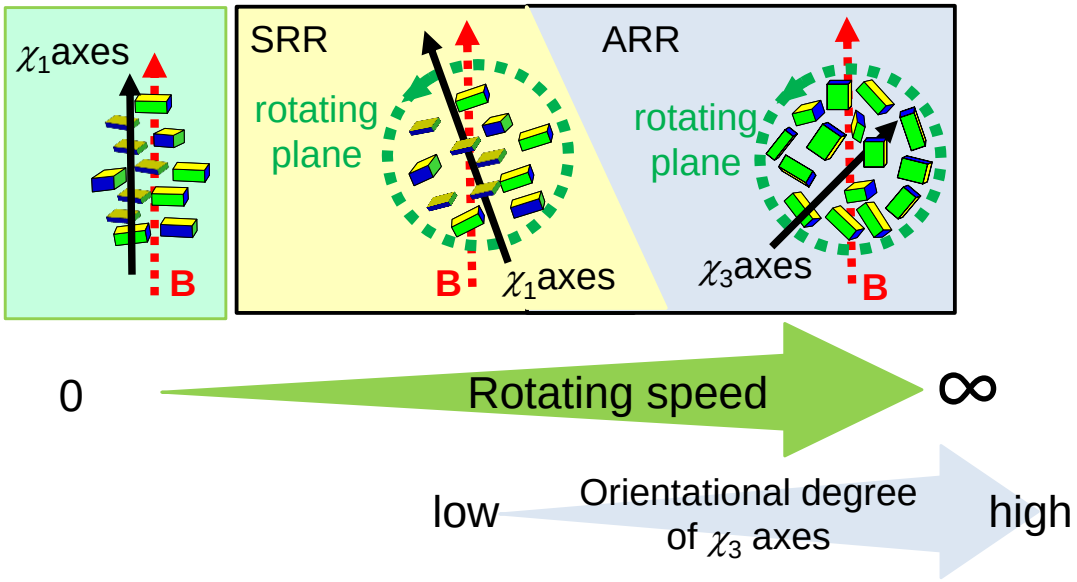

Figure 1.11. Orientational behavior of biaxial microcrystals in rotating magnetic fields with various rotation speeds.

Reference

[1] T. Kimura, M. Yoshino, *Langmuir* **2005**, 21, 4805.

[2] T. Kimura, *Jpn. J. Appl. Phys*. **2009**, 48, 020217.

[3] M. Yamaguchi, S. Ozawa, I. Yamamoto, T. Kimura, *Jpn. J. Appl. Phys*. **2013**, 52, 013003.

[4] T. Kimura, C. Chang, F. Kimura, M. Maeyama, *J. Appl. Crystallogr*. **2009**, 42, 535.

[5] M. Yamaki, S. Horii, M. Haruta, J. Shimoyama, *Jpn. J. Appl. Phys*. **2012**, 51, 010107.

[6] T. Kimura, F. Kimura, M. Yoshino, *Langmuir* **2006**, 22, 3464.

[7] K. Ogawa, Thesis, Iwate University, **2005**.

[8] M. Yamaguchi, S. Ozawa, I. Yamamoto, *Jpn. J. Appl. Phys*. **2010**, 49, 080213.

[9] T. Kimura, G. Song, K. Matsumoto, K. Fujita, F. Kimura, *Jpn. J. Appl. Phys*. **2012**, 51, 040202.

[10] T. Kimura, T. Tanaka, G. Song, K. Matsumoto, K. Fujita, F. Kimura, *Cryst. Growth Des*. **2013**, 13, 1815.

[11] F. Kimura, T. Kimura, W. Oshima, M. Maeyama, K. Aburaya, *J. Appl. Crystallogr*. **2010**, 43, 151.

[12] F. Kimura, K. Mizutani, B. Mikami, T. Kimura, *Cryst. Growth Des*. **2011**, 11, 12.

Chapter 2 Crystal Structure Analysis from *In-Situ* X-ray Diffraction Pattern

2.1 Introduction

In Chapter 1, we demonstrated that two types of fiber patterns can be obtained by an *in-situ* X-ray diffraction measurement on a microcrystalline suspension to which a static magnetic field or a rotating magnetic field (ARR) is applied. One might think that X-ray diffraction patterns of three-dimensionally oriented MOMS can be obtained by performing *in-situ* X-ray diffraction on a microcrystalline suspension to which a magnetic field with modulated or intermittent rotation rather than a simple static or rotating magnetic field is applied. However, this is incorrect. Indeed, under a modulated or intermittent rotation in a magnetic field, microcrystals in the suspension become three-dimensionally oriented. However, to maintain this orientation, the microcrystalline suspension must be constantly rotated. This is not different from rapidly rotating a single crystal about its χ_3 axis, as shown in Figure 2.1(a).

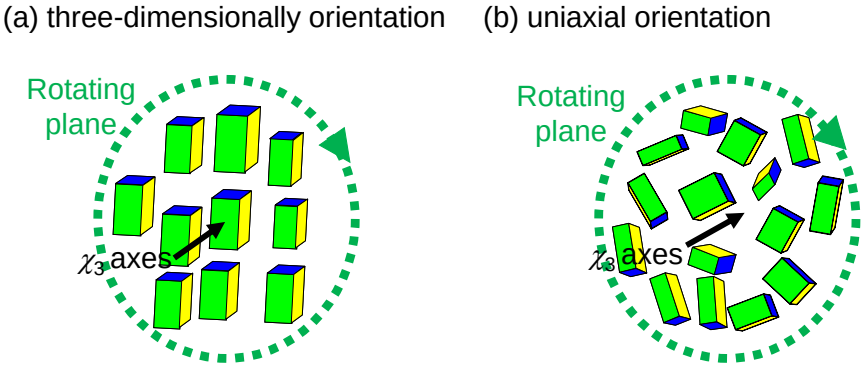

Figure 2.1. Pattern diagram showing *in-situ* X-ray diffraction measurement of (a) microcrystals oriented three-dimensionally and (b) microcrystals only whose χ_3 axes orient. Both microcrystals give rise to the same diffraction pattern because irradiation time of X-ray is longer than the time required for one rotation of the sample.

On the other hand, in a normal X-ray diffraction measurement, X-rays are emitted for a few minutes at a certain angle and then for another few minutes at a slightly different angle; this process is repeated to obtain a number of analysis spots.[1] For three-dimensionally oriented MOMS, patterns obtained by X-ray diffraction are those obtained by measuring a single crystal that has rotated dozens of times around the χ_3 axis (Figure 2.1(a)). This diffraction pattern is the same as those obtained from microcrystals whose χ_3 axes are uniaxially oriented (Figure 2.1(b)). That is, in the MOMS method, although the microcrystals are three-dimensionally oriented, a diffraction pattern similar to that of a single crystal cannot be obtained. For crystal structure analysis, X-ray diffraction patterns of two types of fiber patterns must be used as obtained in Chapter 1.

However, these two diffraction patterns, which are the fiber diffraction patterns, have more advantages than the powder diffraction pattern. (1) Some crystal information (the crystal system, the point group, the crystal space group, and the lattice constant) is easily determined. These informations are decided by the location information of the reciprocal lattice vector. Because combination of two fiber patterns includes more location information of the reciprocal lattice vector than the powder pattern, it is relatively easy to obtain these infomations about crystal. Actually, the determination of these values is the hardest process in crystal structure analysis from a powder X-ray diffraction pattern.[2-5] (2) Intensity of the individual diffraction peak is available. The diffraction peaks cannot be separated every diffraction planes in powder X-ray diffraction pattern. In the case of fiber pattern, many diffraction peaks can be separated in the absence of overlap between the peaks. Furthermore, number of separable diffraction peaks increase using two fiber patterns because the rate of

overlapping peaks are less in both fiber patterns.

So, we think that crystal structure analysis from MOMS method is possible. In this chapter, we report single crystal structure analysis including an indexing from MOMS method. In this study, L-alanine, D-cellobiose, D-arabinitol, urea, and sodium chloride are used as first experimental sample because it is possible to compare with the data in a literature.

2.2 Materials and Methods

2.2.1 Improvement of KU Model χ10-1

The main improvement was made to the magnet portion of the KU model χ10-1. To increase magnetic flux density, the magnets must be set closer together. However, depending on their shapes, the magnets might interrupt diffraction X-rays when they are set closer to each other. The magnets of the KU model χ10-1 were spherical, which is a shape that is likely to block the diffraction X-rays (Figure 2.2(a)); therefore, the shape of the magnets had to be changed. Figure 2.2(b) shows a schematic diagram of the actual magnet portion after changes were made. The shape in Figure 2.2(b) is less likely to block diffraction X-rays compared to spherical magnets. Additionally, we achieved a magnetic flux density of 1.3 T. The rotation unit after improvement was called KU model χ10-2.

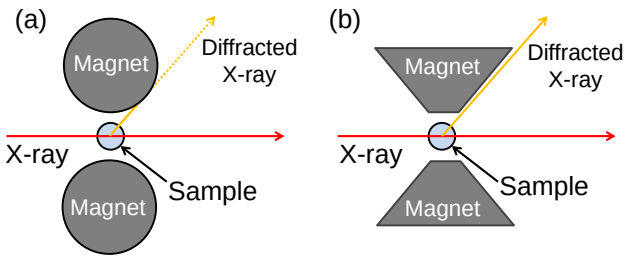

Figure 2.2. Pattern diagram showing shape of magnets on rotating unit. (b) The pyramid magnets can widely pass the diffracted X-ray compared with (a) the sphere magnets.

2.2.2 Preparation of Microcrystalline Suspension

L-alanine crystal purchased from Waco Chemical, Ltd. was pulverized using a mortar and pestle to pass 125-, 75-, 45-, and 20-mesh sieves consecutively. Then, the powder remaining on the 20-mesh sieve was dispersed in ultra-violet (UV)-light-curable monomer (Kyoritsu Chemical XVL-14, viscosity of 12 Pa·s). The concentration of the suspension was ca. 20 wt%. In this study, UV light-curable monomer was used as the suspending medium, because it gives rise to a stable suspension, but the consolidation of this monomer was not carried out. The suspension of D-cellobiose, D-arabinitol, urea, and sodium chloride were prepared in a similar way.

2.2.3 *In-Situ* X-ray Diffraction Measurement

Each of the suspensions of L-alanine D-cellobiose, D-arabinitol, urea, and sodium chloride was poured into a glass capillary (1.5 mm diameter) that was placed at the attachment (KU model χ10-2) composed of a rotating unit and a pair of neodymium magnets of the cuboid (5.0 × 5.0 × 2.0 cm, producing ca. 1.3 T in the center). Then, this attachment was placed on a MAC Science Dip 2020 X-ray diffractometer equipped with an MXP18HF22 rotating anode generator (45 kV, 84 mA). Graphite-monochromated Cu Kα radiation was used and the collimator size was 0.5 mmϕ. Schematic of the experimental setup is shown in Figure 2.3.

The glass capillary set at the attachment was allowed to stand still under a magnetic field, followed by *in-situ* X-ray diffraction measurement for 3 hours with the application of magnetic field kept maintained. Then, the capillary was rotated at 10 rpm for 5 hours, followed by *in-situ* X-ray diffraction measurement for 4 hours in the presence of an applied magnetic field and sustained rotation.

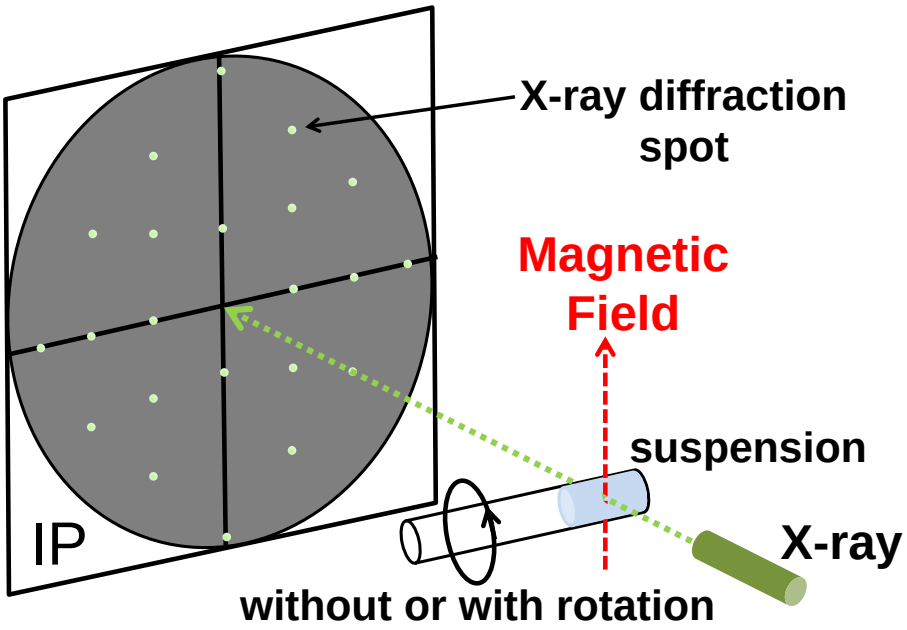

Figure 2.3. Experimental setting of *in-situ* X-ray diffraction measurement of a microcrystalline suspension. A glass capillary containing the microcrystalline suspension stands still or is rotated. When the capillary stands still, the χ_1 axes of microcrystals align uniaxially parallel to the applied field, while when it is rotated, the χ_3 axes of microcrystals uniaxially align parallel to the rotation axis. The X-ray beam is diffracted by the suspension and detected by an imaging plate (IP).

2.3 Results and Discussion

2.3.1 Procedure of Determination of Crystal System

The magnetic susceptibility tensor is described by three principal values χ_1, χ_2, and χ_3, and corresponding principal axes. Here we refer the axes corresponding to χ_1 and χ_3 as easy and hard magnetization axes ($\chi_1>\chi_2>\chi_3$), respectively. For diamagnetic materials all χs take small negative values. For biaxial crystals (triclinic, monoclinic, and orthorhombic crystal systems) three χ values are different; for uniaxial crystals (trigonal, tetragonal, and hexagonal crystal systems) two out of three χ values are equal: $\chi_1>\chi_2=\chi_3$ or $\chi_1=\chi_2>\chi_3$. For the isotropic crystals (cubic crystal system) all the tree χ values are equal.

The crystallographic axes are related to these magnetic axes.[6] For the triclinic crystal system, there is no fixed relation to three magnetic axes. For the monoclinic crystal system, its 2-fold rotation or inversion axis (usually defined as *b* axis) coincides with one of the three magnetic axes. For the orthorhombic crystal system, its three mutually perpendicular 2-fold rotation or inversion axes (that is, *a*, *b*, and *c* axes) correspond to three magnetic axes. For the tetragonal, hexagonal, and trigonal crystal systems, their 4-, 6-, or 3-fold rotation or inversion axes coincide with one of the three magnetic axes. For the cubic crystal system, the directions of the three magnetic axes are not defined.

In Figure 2.3, two types of fiber experiments are defined: in FS (the suspension stands still in a static magnetic field) the easy magnetization axes χ_1s of microcrystals align uniaxially in the direction of the applied magnetic field; in FR (the suspension is rotated in a static magnetic field) the hard magnetization axes χ_3s of microcrystals align uniaxially in the direction parallel to the rotation axis. The X-ray is impinged from the perpendicular direction of the uniaxial axis in both cases. The fiber diffraction patterns obtained by these two fiber experiments (FS and FR) depend on the crystal symmetry of the microcrystal under consideration. The fiber diffraction patterns can be categorized into three cases: (i) case I (spots), (ii) case II (arcs), and (iii) case III (Laue rings).

Investigating these two fiber diffraction patterns, we can determine the crystal system to which the microcrystals under investigation should be assigned. Once the crystal system is determined, the indexing and the determination of the lattice constants and the space group can be made. Flowchart 1 shows the procedure used to determine the crystal system of the microcrystal. Biaxial microcrystals undergo uniaxial orientation about χ_1 under FS experiment, while they undergo uniaxial orientation about

χ_3 under FR experiment. Therefore, if both fiber diffraction patterns belong to case I, the microcrystal under investigation is assigned to the biaxial crystal system. On the other hand, if one of the fiber diffraction patterns belongs to case I and the other to case II, the microcrystal is assigned to the uniaxial system. If both patterns belong to case III, the microcrystal is assigned to the isotropic system.

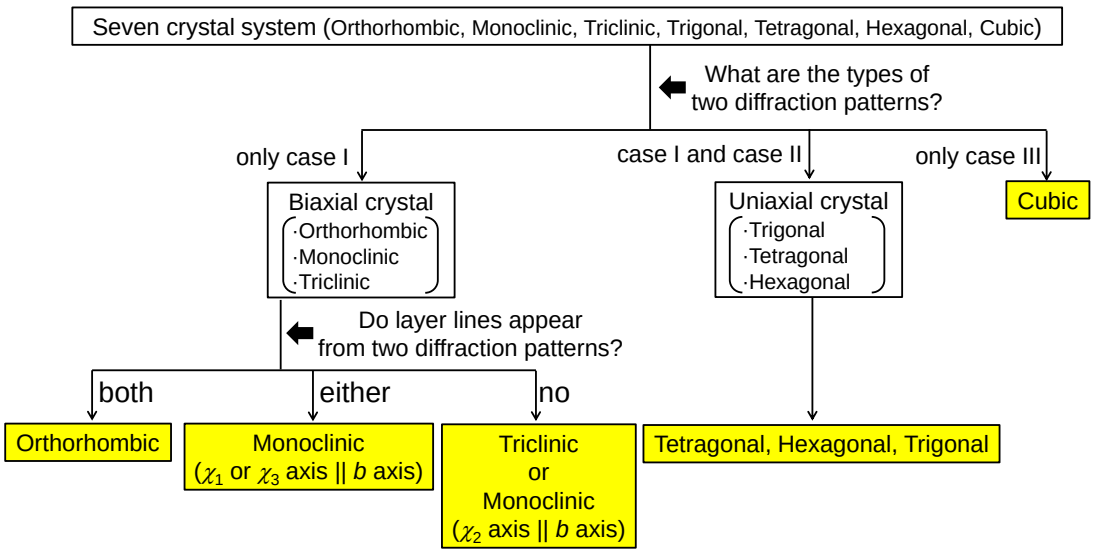

Flowchart 1. This is the flowchart to show the procedure used to determine the crystal system of the sample. First, the types (case I (spots), case II (arcs), case III (rings)) of obtained two diffraction patterns are investigated. Next, the presence or absence of the layer lines about the diffraction pattern of case I is investigated.

Let us consider the case where the microcrystal is assigned to biaxial crystal. If both of two case-I diffraction patterns exhibit layered lines, the microcrystal is assigned to the orthorhombic crystal system because the χ_1, χ_2, and χ_3 axes coincide with three crystallographic axes in the case of orthorhombic system.[6] If the diffraction from FS experiment exhibit layered lines, but that from FR experiment does not, or if the diffraction from FS experiment does not exhibit layered lines, but that from FR experiment does, then the microcrystal is assigned to the monoclinic crystal system.

In the former case, the χ_1 axis coincides with the *b* axis (2-fold axis) and in the latter case, the χ_3 axis coincides with the *b* axis. On the other hand, if neither FS nor FR experiments give rise to layered lines, the microcrystal is assigned to the triclinic crystal system or the monoclinic crystal system with the χ_2 axis coinciding with the *b* axis. Next, let us consider the case where the microcrystal is assigned to uniaxial crystal. In uniaxial crystal, all case I pattern exhibits layered lines. Once the crystal system is determined, the further process of determination of lattice constants and the space group is greatly facilitated.

2.3.2 Procedure of Determination of Lattice Constants and Space Group

The lattice constants of sample are determined from two fiber diffraction patterns. The determination of the lattice constants becomes easier than the determination from the powder pattern because the indexing is facilitated by use of two fiber diffraction patterns. In addition, in the case that the fiber diffraction pattern has layer lines, the determination of the lattice constants becomes much more facilitated because the length of the lattice is easily obtained when the fiber diffraction pattern is available.

Finally we consider the determination of the point group and the space group. The point group is commonly determined by the process of scaling analysis at single crystal structure analysis,[7] but this is not the case for fiber patterns because the π rotation of crystal cannot be distinguished in the fiber pattern produced by magnetic orientation. So, the point group is determined from the extinction rule. Using the extinction rule, possible candidates for the point group and the space group are predicted.

2.3.3 Demonstration of Determination of Crystal System, Lattice Constant, Point Group, and Space Group

In this section, we show how the procedure described in the previous section is applied to an actual case. *In-situ* X-ray diffraction patterns measured for FS (without rotation) and FR (with rotation) of L-alanine, D-cellobiose, D-arabinitol, urea, and sodium chloride are shown in Figure 2.4(a)~(e), respectivly. The crystal system of each of these samples was determined from the X-ray diffraction patterns using Flowchart 1. First, the crystal system of L-alanine was determined. Because the diffraction spots appear in both FS and FR patterns in Figure 2.4(a), L-alanine is determined as biaxial. Furthermore, because the layered lines are observed in both patterns, L-alanine is assigned to belong to the orthorhombic crystal system. Next, crystal system of D-cellobiose was determined. Because the diffraction spots appear in both FS and FR patterns in Figure 2.4(b), D-cellobiose is determined as biaxial. Furthermore, because the layered lines are observed in only one pattern, D-cellobiose is assigned to belong to the monoclinic crystal system (χ_1 or χ_3 axis || *b* axis). Next, the crystal system of D-arabinitol was determined. Because the diffraction spots appear in both FS and FR patterns in Figure 2.4(c), D-arabinitol is determined as biaxial. Furthermore, because the layered lines are not observed in both patterns, D-arabinitol is assigned to belong to the triclinic or monoclinic (χ_2 axis || *b* axis) crystal system. Next, the crystal system of urea was determined. Because the diffraction spots appear in only FS pattern in Figure 2.4(d), urea is determined as uniaxial. Finally, the crystal system of sodium chloride was determined. Because the diffraction spots do not appear in both FS and FR patterns in Figure 2.4(e), sodium chloride is assigned to belong to the cubic crystal system.

(a)L-alanine

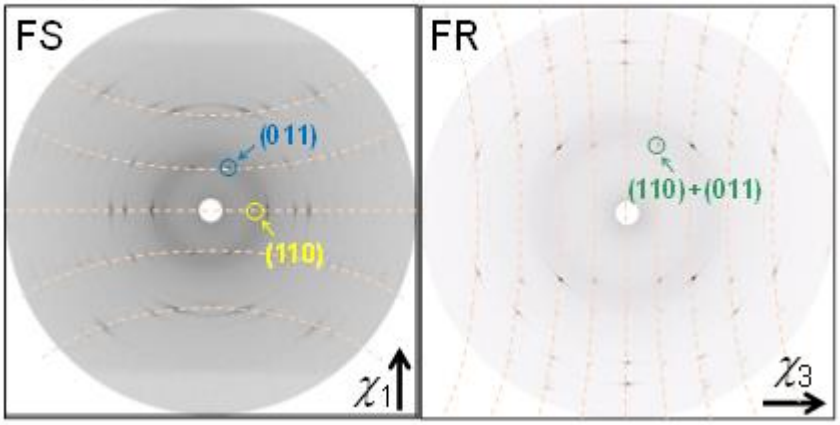

(b)D-cellobiose

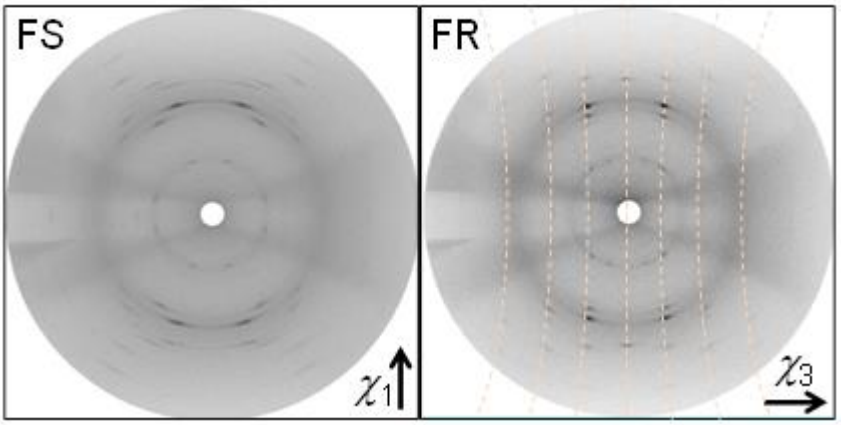

(c)D-arabinitol

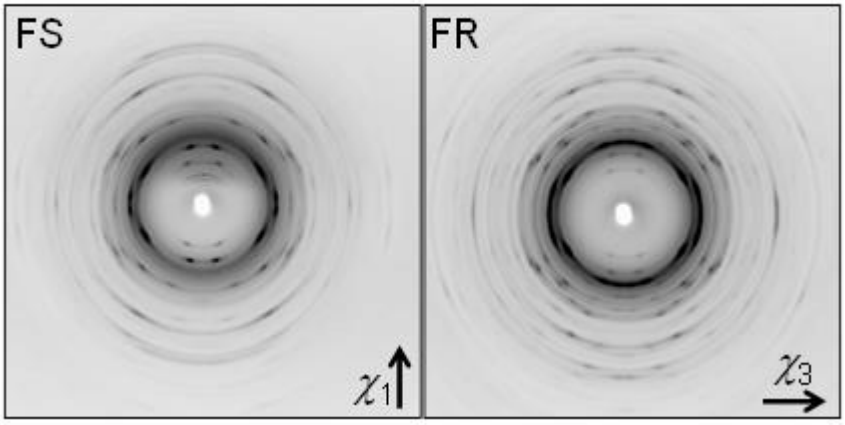

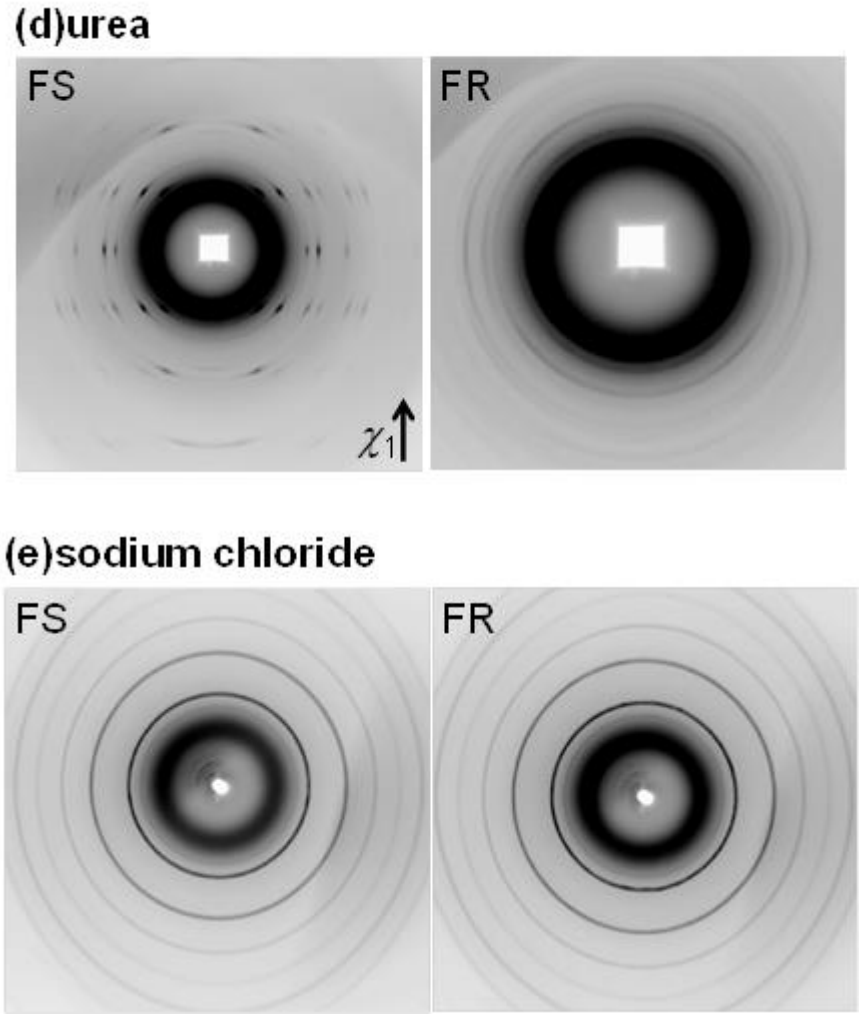

Figure 2.4. X-ray diffraction images obtained for *in-situ* X-ray diffraction measurement of microcrystalline suspension of (a) L-alanine, (b) D-cellobiose, (c) D-arabinitol, (d) urea, and (e) sodium chloride without rotation (FS) and rotation (FR) under a static magnetic field. Broken lines mean the layer lines.

The crystal lattice constants are determined from these two X-ray diffraction patterns. We choose L-alanine as an example for which the determination of the crystal lattice parameters is demonstrated. Because L-alanine is orthorhombic ($\alpha = \beta = \gamma = 90^{\circ}$) the lengths of the crystal axes corresponding to χ_1 and χ_3 axes are determined from the distance between the layers. In fact, the lengths of crystal axes corresponding

to the χ_1 and χ_3 axes are ca. 5.8 Å and 12.4 Å, respectively. Then, using these values, the indexing of diffraction spots in Figure 2.4(a) is performed. The lattice constants are obtained from the scattering angle of indexed diffraction spots. The lengths of three axes are determined as a=6.04 Å, b=12.37 Å, and c=5.79 Å. The relationship to the magnetic axes is $a \| \chi_2$, $b \| \chi_3$, $c \| \chi_1$.

Finally, the space group of the crystal is determined using the extinction rule. The orthorhombic crystal system includes three point groups, *mmm*, *mm*2, and 222, to which several space groups belong. In Figure 2.4(a), the extinctions about (h00), (0k0), and (00l) planes are observed for these h, k, and l values, h=2n-1, k=2n-1, and l=2n-1 (n is an integer number). Therefore, it is concluded that the space group of the crystal is $P2_12_12_1$. This conclusion is in agreement with that of L-alanine crystal reported in literature.[8]

2.3.4 Analysis of Diffraction Intensities

The intensities of the observed diffraction spots in Figure 2.4(a) are compared with the intensities predicted based on the reported structure of L-alanine[9] in order to evaluate the present method. Azimuthal scan was performed on each diffraction pattern and the integration of the peak was made using a fitting of the azimuthal profile with a pseudo-Voigt function, whereby Lorentz correction was made. From the diffraction pattern of FS experiment (Figure 2.4(a)), the intensities of independent 24 diffraction spots were obtained. On the other hand, from the diffraction pattern of FR experiment (Figure 2.4(a)), the intensities of independent 26 diffraction spots were obtained. In each diffraction pattern, there are overlapping spots that are contributions from different (*hkl*) planes. This overlap problem is dissolved by comparing both

diffraction patterns of FS and FR. For example, (110) and (011) planes overlap in the diffraction pattern of FR (Figure 2.4(a)), but they do not in the diffraction pattern of FS (Figure 2.4(a)). After resolving the overlapping, we obtained 44 independent diffraction spots from FS and FR.

The observed intensities (F_O) were evaluated by comparing with those (F_C) calculated by Shelx-97 using the crystallographic data of L-alanine reported in the literature, where the temperature factor and the anisotropic temperature factors were fixed. The results are summarized in Table 2.1 and Figure 2.5. The *R*1 and *wR*2 values were 18.84 and 46.27 %, respectively when 44 independent intensity data are used. This result is not satisfactory. Large *R* values are mainly attributed to a poor quality of the data from the FS measurement. If the calculation is performed on FS and FR data separately, we obtain 28.90 and 60.33 % for FS, while we obtain 10.29 and 28.83 %, respectively, for *R*1 and *wR*2. These results are summarized in Table 2.2 and Figure 2.6.

A poor quality of FS data can be explained as follows: In the FR measurement, the suspension is rotating during the X-ray measurement, while in the FS measurement, the suspension is still in the magnetic field. By rotation, the χ_1 and χ_2 axes change their directions, then every particle can contribute to diffract, allowing the improvement of the data quality. There is an inhomogeneity of the magnetic field produced between two poles of permanent magnet. By rotation, this inhomogeneity is partially averaged. In addition, larger microcrystals in the suspension may sink during the X-ray measurement. By rotation, the effect due to the sinking can be partially cancelled. All these advantages of FR measurement that contribute to improve the data quality of diffraction cannot be expected in FS measurement.

The quality of the data from FS measurement might be improved by oscillation of the suspension about the direction parallel to the applied magnetic field. Also the quality might be improved by changing the design of the magnetic circuit so as to obtain a good magnetic homogeneity. The sinking problem may be solved if we choose such a suspending liquid that has a density close to the suspended microcrystals and/or has a viscosity high enough to prevent the sinking.

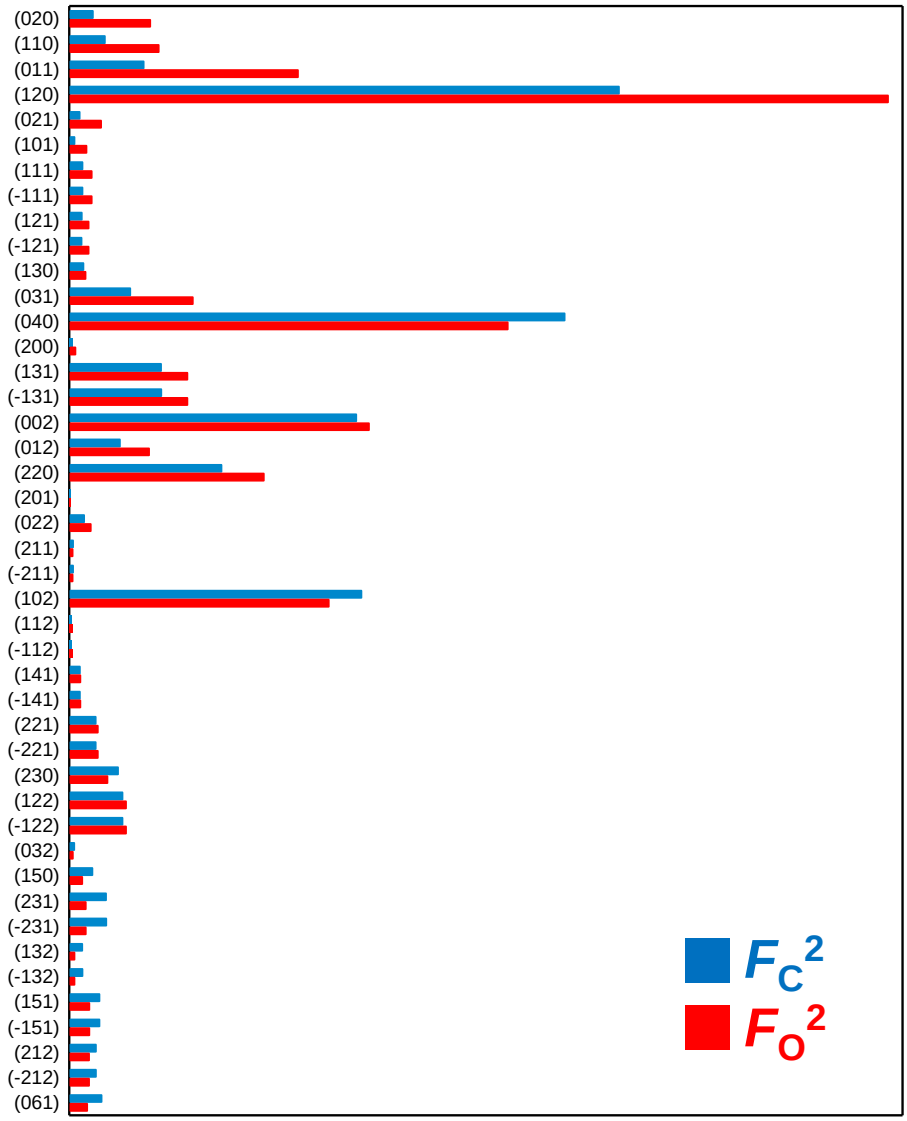

Figure 2.5. The comparison between F_C^2 and F_O^2 for each of diffraction peaks. F_O^2 was obtained from the combination of two fiber diffraction patterns.

Table 2.1. The comparison between F_C^2 and F_O^2 for each of diffraction peaks. F_O^2 was obtained from the combination of two fiber diffraction patterns.

h	k	l	F_C^2	F_O^2
0	2	0	221.03	745.26
1	1	0	330.11	821.59
0	1	1	685.10	2092.18
1	2	0	5019.40	7474.00
0	2	1	101.03	296.53
1	0	1	53.43	163.11
1	1	1	126.62	210.04
-1	1	1	127.00	210.04
1	2	1	119.82	182.93
-1	2	1	118.95	182.93
1	3	0	135.55	154.36
0	3	1	562.57	1131.78
0	4	0	4523.37	4004.88
2	0	0	30.34	62.42
1	3	1	842.50	1082.61
-1	3	1	845.01	1082.61
0	0	2	2624.04	2740.22
0	1	2	467.68	733.40
2	2	0	1395.10	1781.31
2	0	1	0.04	0.00
0	2	2	142.50	202.28
2	1	1	41.48	36.12
-2	1	1	40.80	36.12
1	0	2	2671.33	2373.02
1	1	2	19.70	29.81
-1	1	2	19.81	29.81
1	4	1	103.35	107.22
-1	4	1	103.41	107.22
2	2	1	247.44	266.04
-2	2	1	247.20	266.04
2	3	0	450.64	353.34
1	2	2	492.14	523.00
-1	2	2	492.18	523.00
0	3	2	51.88	39.58
1	5	0	216.95	125.08
2	3	1	342.08	156.39
-2	3	1	342.28	156.39
1	3	2	125.12	54.53
-1	3	2	125.54	54.53
1	5	1	280.81	187.81
-1	5	1	280.32	187.81
2	1	2	248.83	186.44
-2	1	2	249.78	186.44
0	6	1	301.12	169.94

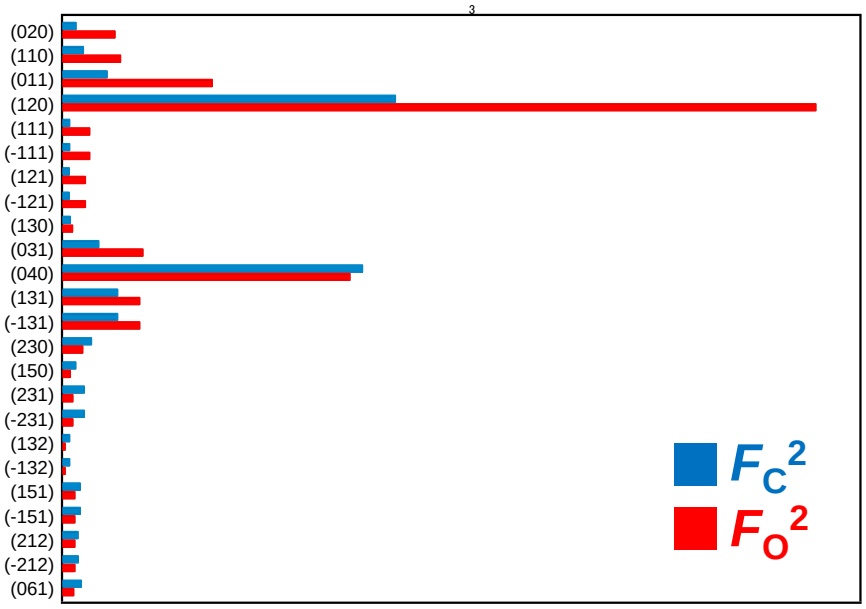

(a)FS

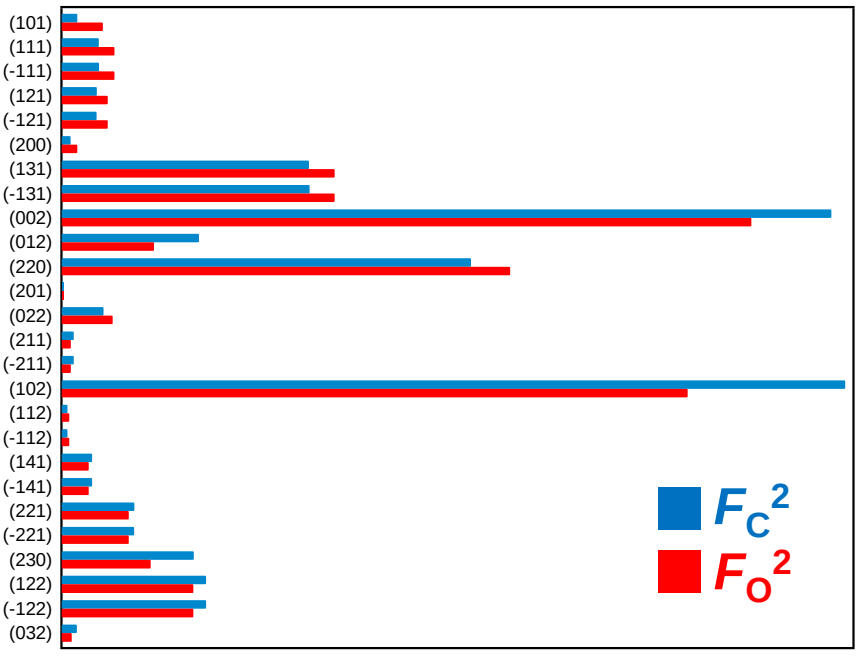

(b)FR

Figure 2.6. The comparison between F_C^2 and F_O^2 for each of diffraction peaks. F_O^2 was obtained from (a) the fiber diffraction pattern without rotation (FS) and (b) the fiber diffraction pattern with rotation (FR).

Table 2.2. The comparison between F_C^2 and F_O^2 for each of diffraction peaks. F_O^2 was obtained from (a) the fiber diffraction pattern without rotation (FS) and (b) the fiber diffraction pattern with rotation (FR).

(a)FS

h	*k*	*l*	F_C^2	F_O^2
0	2	0	221.03	807.14
1	1	0	330.11	889.39
0	1	1	685.10	2264.83
1	2	0	5019.40	11337.11
1	1	1	126.62	422.93
-1	1	1	127.00	422.93
1	2	1	119.82	357.71
-1	2	1	118.95	357.71
1	3	0	135.55	167.10
0	3	1	562.57	1225.17
0	4	0	4523.37	4335.35
1	3	1	842.50	1173.77
-1	3	1	845.01	1173.77
2	3	0	450.64	317.38
1	5	0	216.95	135.40
2	3	1	342.08	169.29
-2	3	1	342.28	169.29
1	3	2	125.12	59.03
-1	3	2	125.54	59.03
1	5	1	280.81	203.30
-1	5	1	280.32	203.30
2	1	2	248.83	201.82
-2	1	2	249.78	201.82
0	6	1	301.12	183.96

(b)FR

h	*k*	*l*	F_C^2	F_O^2
1	0	1	53.43	139.96
1	1	1	126.62	180.22
-1	1	1	127.00	180.22
1	2	1	119.82	156.96
-1	2	1	118.95	156.96
2	0	0	30.34	53.56
1	3	1	842.50	930.45
-1	3	1	845.01	930.45
0	0	2	2624.04	2351.23
0	1	2	467.68	314.70
2	2	0	1395.10	1528.44
2	0	1	0.04	0.00
0	2	2	142.50	173.56
2	1	1	41.48	30.99
-2	1	1	40.80	30.99
1	0	2	2671.33	2133.75
1	1	2	19.70	25.58
-1	1	2	19.81	25.58
1	4	1	103.35	92.00
-1	4	1	103.41	92.00
2	2	1	247.44	228.27
-2	2	1	247.20	228.27
2	3	0	450.64	303.18
1	2	2	492.14	448.75
-1	2	2	492.18	448.75
0	3	2	51.88	33.96

2.4 Summary

To conclude, we have demonstrated the potential of MOMS method as a means to determine structure by a single crystal X-ray analyses. In this study, a microcrystalline powder of L-alanine was used for the purpose of demonstration. *In-situ* X-ray diffraction measurement was performed on an L-alanine microcrystalline suspension that was subjected to a static or a rotating magnetic field. From the two diffraction patterns obtained, the space group and the lattice constants of L-alanine were determined with no knowledge. The observed 44 independent diffraction intensities were in good agreement with the values calculated from the single crystal data.

Reference

[1] B. D. Cullity, S. R. Stock, *Elements Of X Ray Diffraction*, 1956.

[2] W. I. F. David, K. Shankland, L. B. McCusker, C. Baerlocher, Editors. *Structure Determination from Powder Diffraction Data*, IUCr Monographs on Crystallography 13, Oxford University Press, **2002**.

[3] K. D. M. Harris, *Cryst. Growth Des.* **2003**, 3, 887.

[4] K. D. M. Harris, E. Y. Cheung, *Chem. Soc. Rev.* **2004**, 33, 526.

[5] R. Shirley, *Overview of powder-indexing program algorithms (history and strengths and weaknesses)*, IUCr Computing Commission 48, **2006**.

[6] J. F. Nye, *Physical Properties of Crystals*, Clarendon Press: Oxford, 1985; Chapter 1.

[7] Evans, P. *Acta Crystallogr*. **2006**, D62, 72.

[8] H. J. Simpson Jr., R. E. Marsh, *Acta Crystallogr*. **1966**, 20, 550.

[9] Wilson, C. C.; Myles, D.; Ghosh, M.; Johnson, L. N.; Wang, W. *New J. Chem.* **2005**, 29, 1318.

Chapter 3 Determination of Anisotropic Magnetic Susceptibility from *In-Situ* X-ray Diffraction Pattern

3.1 Introduction

Three-dimensional alignment occurs to biaxial crystals by application of time-dependent magnetic field.[1-4] The square intensity of the orientation fluctuation about each of these axes is proportional to $(\chi_2\text{-}\chi_3)^{-1}$, $(\chi_1\text{-}\chi_3)^{-1}$, and $(\chi_1\text{-}\chi_2)^{-1}$, respectively, as well as to the parameters defining the time-dependent magnetic field used.[4,5]

When a modulated rotating magnetic field, whose rotating speed are chosen as ω_s and ω_q as shown in Figure 5, is used, the orientational fluctuations $<\delta_1^2>$, $<\delta_2^2>$, $<\delta_3^2>$ about each magnetization axis are described as follows:[4]

$$\langle\delta_1^2\rangle = \frac{C\{\pi + (r_\omega - 1)\alpha\}}{(\chi_2 - \chi_3)\{\pi + (r_\omega - 1)(\alpha - \sin\alpha)\}}$$
$$\langle\delta_2^2\rangle = \frac{C\{\pi + (r_\omega - 1)\alpha\}}{(\chi_1 - \chi_3)\{\pi + (r_\omega - 1)(\alpha + \sin\alpha)\}}$$
$$\langle\delta_3^2\rangle = \frac{C\{\pi + (r_\omega - 1)\alpha\}}{2(\chi_1 - \chi_2)(r_\omega - 1)\sin\alpha}, \tag{3.1}$$

where $r_\omega = \omega_q/\omega_s$ and α is the angle defined in the general introduction. The fluctuations determined by eq. (3.1) for the values of $\alpha = 10^o$, $\alpha = 90^o$ are shown in Figure 3.1. In the diffraction method, it is preferable to have the orientational fluctuations of each axis equal to each other. From Figure 3.1, this condition is satisfied when $<\delta_1^2>=<\delta_3^2>$. From eq. (3.1), this condition is described as follows:

$$\frac{\sin\alpha\,(r_\omega - 1)}{2\{\pi + (r_\omega - 1)(\alpha - \sin\alpha)\}} = \frac{\chi_2 - \chi_3}{\chi_1 - \chi_2} = r_\chi.$$

(3.2)

We find that the ratio r_χ=(χ_2-χ_3)/(χ_1-χ_2) is required for determination of the optimal condition of the orientation.

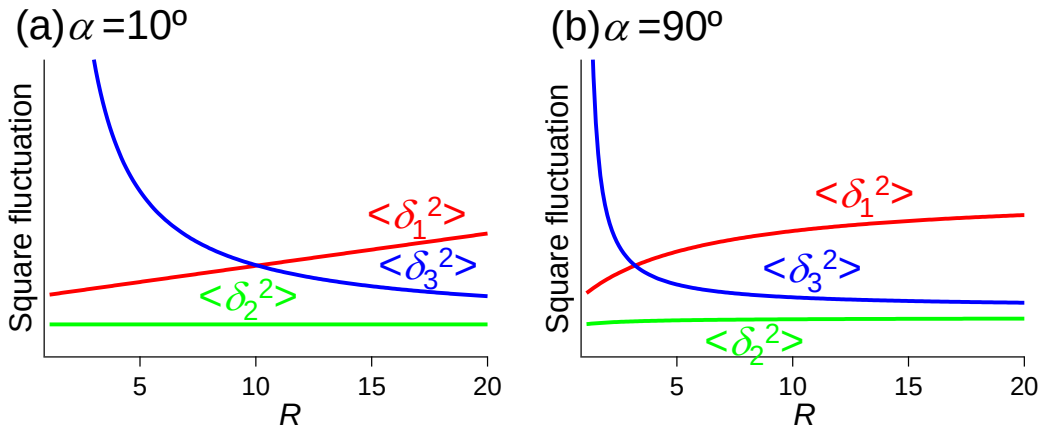

Figure 3.1. Mean square fluctuation of microcrystals subjected to a time-dependent elliptic magnetic field. $<\delta_1^2>$, $<\delta_2^2>$, and $<\delta_3^2>$ indicate the means square fluctuation about χ_1, χ_2, and χ_3 axis, respectively.

On the other hand, in an intermittently rotating magnetic field (repetition of a stop (duration of t_{stop}) and a 180° rotation (duration of t_{rot} at rotation speed of ω)) as shown in Figure 6, the orientational fluctuations, $<\delta_1^2>$, $<\delta_2^2>$ and $<\delta_3^2>$, are described as follows:

$$\langle\delta_1^2\rangle = \frac{C(R+1)}{\chi_2 - \chi_3}, \langle\delta_2^2\rangle = \frac{C(R+1)}{(2R+1)(\chi_1 - \chi_3)}, \text{and } \langle\delta_3^2\rangle = \frac{C(R+1)}{2R(\chi_1 - \chi_2)},$$

(3.3)

respectively, where R=t_{stop}/t_{rot}.[4] This is shown in Figure 3.2. It can be observed in Figure 3.2 that the most preferable orientation in an intermittently rotating magnetic

field occurs when $<\delta_1^2>=<\delta_3^2>$. Here, from eq (3.3), $2R=(\chi_2-\chi_3)/(\chi_1-\chi_2)$ should be satisfied. Here again, we find that the ratio $r_\chi=(\chi_2-\chi_3)/(\chi_1-\chi_2)$ is required for determination of the optimal condition of the orientation. Incidentally, a method for obtaining r_χ from the X-ray diffraction patterns of the microcrystals oriented in a static or rotating magnetic field has been theoretically proposed. We briefly show below the result obtained by the theory.[5] Therefore, r_χ can be obtained using the *in-situ* X-ray diffraction patterns obtained in chapter 1. In this chapter, we demonstrate the determination of the ratio r_χ of L-alanine and D-mannitol crystals by means of *in-situ* X-ray measurement of the suspension of their microcrystalline powder.

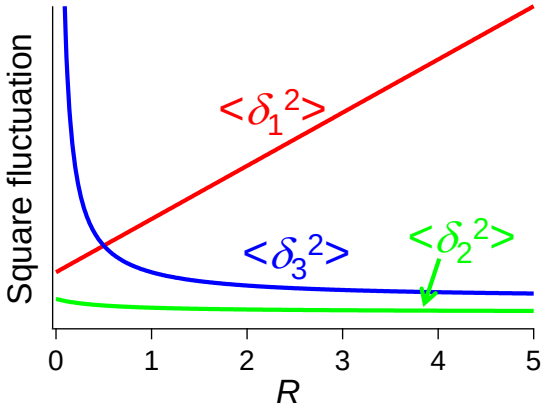

Figure 3.2. Square fluctuation of microcrystals subjected to an intermittent rotating magnetic field. $<\delta_1^2>$, $<\delta_2^2>$, and $<\delta_3^2>$ indicate the square fluctuation about χ_1, χ_2, and χ_3 axis, respectively.

3.2 Theory[5,6]

We obtain eq. (3.4) from eq. (1.3).

$$\frac{H_{\mathrm{R}}^2}{f_{\mathrm{R}}^2} = \frac{C}{\chi_1 - \chi_3} + \frac{C(\chi_1 - \chi_2)}{(\chi_1 - \chi_3)(\chi_2 - \chi_3)} \sin^2 \Phi_{\mathrm{R}} \tag{3.4}$$

If $H_{\mathrm{R}}^2/f_{\mathrm{R}}^2$ is plotted as a function of $\sin^2\Phi_{\mathrm{R}}$, we obtain a line. The *y*-intercept and the slope are equal to $C/(\chi_1\text{-}\chi_3)$ and $C(\chi_1\text{-}\chi_2)/(\chi_1\text{-}\chi_3)(\chi_2\text{-}\chi_3)$, represented (Figure 3.3). By taking the ratio of these quantities, we obtain $r_\chi=(\chi_2\text{-}\chi_3)/(\chi_1\text{-}\chi_2)$. Hereafter, we simplify the expression (3.4) as follows by putting $a=C(\chi_1\text{-}\chi_2)/(\chi_1\text{-}\chi_3)(\chi_2\text{-}\chi_3)$ and $b=C/(\chi_1\text{-}\chi_3)$:

$$\frac{H_{\mathrm{R}}^2}{f_{\mathrm{R}}^2} = a \sin^2 \Phi_{\mathrm{R}} + b. \tag{3.5}$$

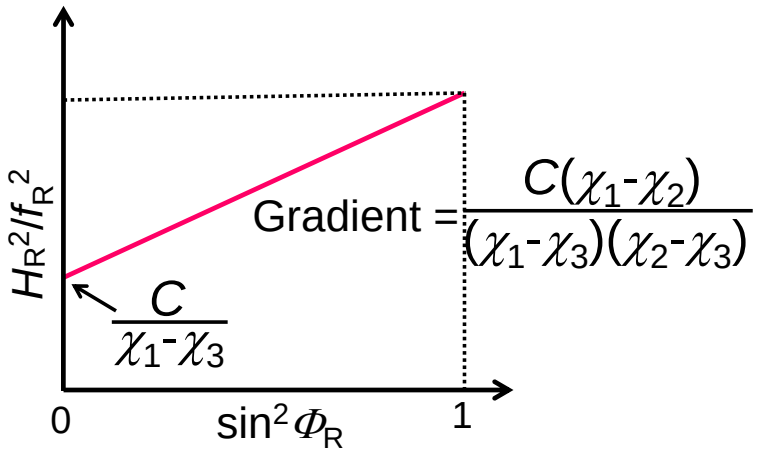

Figure 3.3. Plot of $H_{\mathrm{R}}^2/f_{\mathrm{R}}^2$ as a fuction of $\sin^2\Phi_{\mathrm{R}}$. This plot indicates a line whose *y*-intercept is $C/(\chi_1\text{-}\chi_3)$ and slope is $C(\chi_1\text{-}\chi_2)/(\chi_1\text{-}\chi_3)(\chi_2\text{-}\chi_3)$.

3.3 Materials and Methods

3.3.1 Preparation of Microcrystalline Suspension

L-Alanine crystal (Wako Chemical, Ltd.) was pulverized using a mortar and pestle to pass 125-, 75-, and 20-mesh sieves consecutively, and the powder remaining on the 20-mesh sieve was dispersed in ultra-violet (UV)-light-curable monomer (Kyoritsu Chemical XVL-14). The concentration was 20.0wt%. D-Mannitol crystal (Wako Chemical, Ltd.) was passed 125-, 75-, and 20-mesh sieves consecutively and the powder remaining on the 20-mesh sieve was dispersed in polyethylene glycol (PEG#400). The concentration was 20.0wt%.

3.3.2 *In-Situ* X-ray Diffraction Measurement

The suspension of L-alanine was poured into a glass capillary and placed at a rotating unit (KU model χ10-1) equipped with a pair of sphere-type neodymium magnets (3 cmϕ, producing ca. 0.7 T in the center). Schematic of the experimental setup is shown in Figure 3.4. Then, the rotating unit was placed in a MAC Science Dip 2000 X-ray diffractometer equipped with an MXP18HF22 rotating anode generator (45 kV, 84 mA). Graphite-monochromated Cu Kα radiation was used and the collimator size was 0.5 mmϕ. Divergence of the beam was ca. 0.19°. The glass capillary containing the L-alanine suspension was rotated at 10 rpm. After 6 hours, the suspension was subjected to *in-situ* X-ray diffraction measurement for 3 h with the application of magnetic field and rotation kept maintained.

The suspension of D-mannitol was poured into a glass capillary and placed on a rotating unit (KU model χ10-1) equipped with a pair of sphere-type neodymium magnets (3 cmϕ, producing ca. 1.1 T in the center). Then, the rotating unit was placed

in a MAC Science Dip 2000 X-ray diffractometer equipped with an MXP18HF22 rotating anode generator (45 kV, 84 mA). Graphite-monochromated Cu Kα radiation was used and the collimator size was 0.9 mmϕ. Divergence of the beam was ca. 0.5°. The glass capillary containing the D-mannitol suspension was rotated at 20 rpm. After one hour, the suspension was subjected to *in-situ* X-ray diffraction measurement for 45 min with the application of magnetic field and rotation kept maintained.

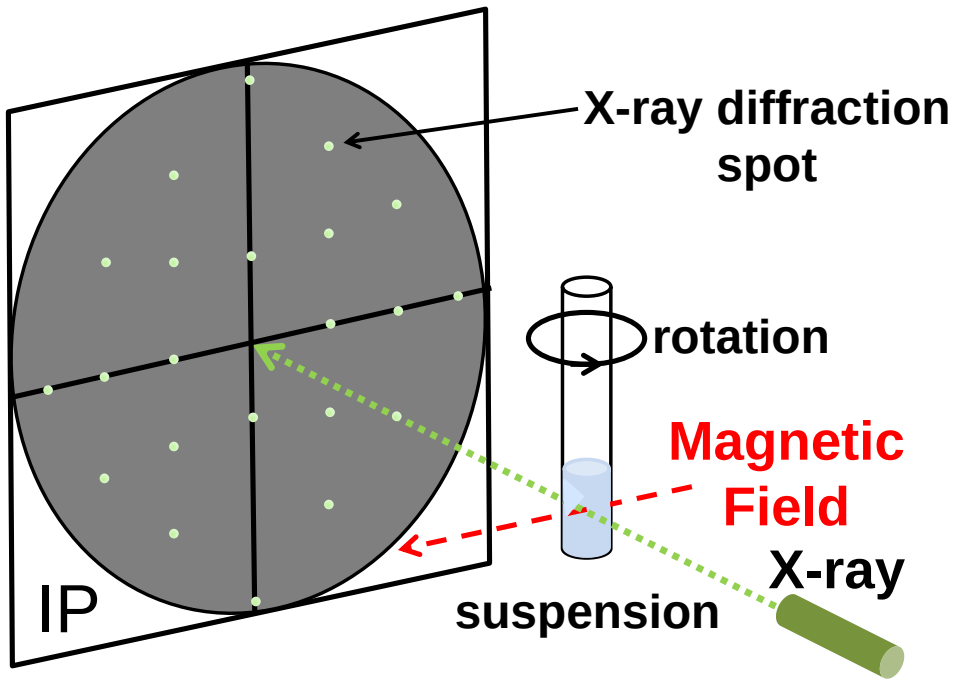

Figure 3.4. Schematic of experimental setting of *in-situ* X-ray diffraction measurement of a microcrystalline suspension. A glass capillary containing the microcrystalline suspension is rotated under a magnetic field. The X-ray beam is diffracted by the suspension and detected by an imaging plate (IP).

3.3.3 Preparation and X-ray Diffraction Measurement of L-Alanine MOMA

Crystal of L-alanine was pulverized using a mortar and pestle to pass 125-, 75-, 45-, and 20-mesh sieves consecutively, and the powder remaining on the 20-mesh sieve was used. The powder was suspended in UV-curable monomer (XVL-14). The

concentration of the suspension was 10.0 wt%. A small amount of suspension was poured into a plastic container and mounted on a sample-rotating unit (KU model χ10-2) placed in an electromagnet (1 T), followed by an intermittent rotation. The intermittent rotation was a repetition of a stop (0.5 s) followed by a rotation (rotating speed of ω) of 180°. After 3 hours, the UV light was irradiated to photopolymerize the monomer and to consolidate the achieved alignment. Five different rotating speeds, ω =10, 15, 30, 60, and 90 rpm, were used to prepare five MOMAs.

Next, L-alanine MOMAs were subjected to X-ray diffraction measurement using a Rigaku RAXIS RAPID II system equipped with an imaging plate with graphite-monochromatized Cu Kα radiation. The collimator size was 0.5 mmϕ.

3.4 Results and Discussion

3.4.1 *In-Situ* X-ray Diffraction Pattern

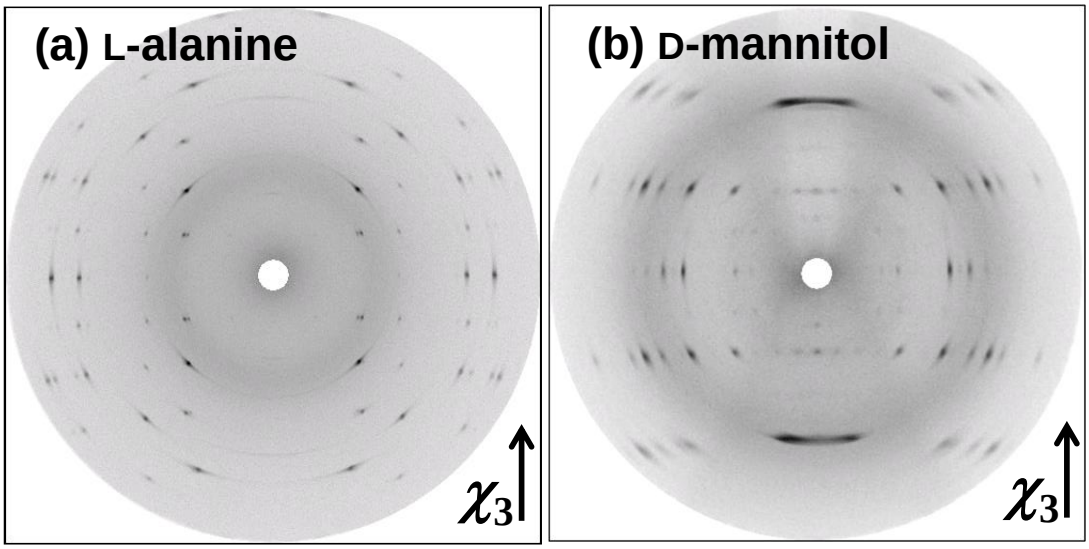

Figure 3.5. X-ray diffraction images of magnetically oriented microcrystalline suspension of (a) L-alanine and (b) D-mannitol. The χ_3 axes of microcrystals align in the direction of sample rotating axis.

The X-ray diffraction pattern of the suspensions of L-alanine (orthorhombic, space group $P2_12_12_1$, a=6.03 Å, b=12.34 Å, c=5.78 Å)[7] is shown in Figure 3.5(a). The meridional direction corresponds to the sample rotating axis, that is, the hard magnetization axis (χ_3). All the three magnetic axes correspond to the crystallographic axes in the case of the orthorhombic system. In the case of L-alanine, χ_1, χ_2, and χ_3 axes coincide with the *c*, *a*, and *b* axes, respectively. Therefore, the *b* axis lies in the meridional direction and the *a* and *c* axes lie in the equator in Figure 3.5(a). Using this information, the diffraction spots are indexed and the half widths H_E are determined. The results are summarized in Table 3.1(a). A similar procedure is applied to the diffraction data of D-mannitol (orthorhombic, space group $P2_12_12_1$, a=8.67 Å, b=16.88 Å, c=5.56 Å)[8] shown in Figure 3.5(b). In the case of D-mannitol, it was understood from this experiment that χ_1, χ_2, and χ_3 axes coincide with the *b*, *c*, and *a* axes, respectively. Therefore, the *a* axis lies in the meridional direction and the *b* and *c* axes lie in the equator. Using this information, the diffraction spots are indexed and the half widths H_Es are determined. The results are summarized in Table 3.1(b).

Table 3.1. Experimental results for the half width for {*hkl*} planes of (a) L-alanine and (b) D-mannitol. The calculated results of the length *G* of reciprocal lattice vector and the angles Θ_R and Φ_R characterizing the direction of the reciprocal vector **G** are shown. The quantity is the correction factor (Eq. (1.4)).

(a)

{*hkl*}	2θ/deg	G/Å^{-1}	Θ_R/deg	Φ_R/deg	f_R^2	H_E/deg
{002}	30.91	0.346	90.0	0.0	1.076	1.01
{012}	31.75	0.355	76.8	0.0	1.086	1.04
{102}	34.36	0.384	90.0	25.6	1.096	1.07
{122}	37.39	0.416	67.1	25.6	1.138	1.04
{111}	22.46	0.253	71.3	43.8	1.044	1.40
{121}	25.73	0.289	55.9	43.8	1.078	1.29
{131}	30.47	0.341	44.6	43.8	1.163	1.21
{141}	36.14	0.403	36.5	43.8	1.374	1.24
{221}	36.58	0.408	66.6	62.5	1.132	1.19
{120}	20.54	0.232	45.7	90.0	1.066	1.58
{140}	32.56	0.364	27.1	90.0	1.609	1.52
{220}	33.01	0.369	64.0	90.0	1.111	1.25
{230}	36.90	0.411	53.8	90.0	1.182	1.22

(b)

{*hkl*}	2θ/deg	G/Å^{-1}	Θ_R/deg	Φ_R/deg	f_R^2	H_E/deg
{120}	14.63	0.165	45.8	0.0	1.033	3.77
{130}	18.78	0.212	57.0	0.0	1.039	3.74
{140}	23.42	0.264	64.1	0.0	1.054	3.46
{150}	28.34	0.318	68.7	0.0	1.074	3.42
{131}	24.72	0.278	65.5	45.3	1.059	4.19
{021}	19.09	0.215	90.0	56.6	1.028	4.41
{121}	21.69	0.244	61.8	56.6	1.048	4.22
{221}	28.13	0.316	43.0	56.6	1.145	4.21
{011}	16.77	0.189	90.0	71.8	1.022	4.67

3.4.2 Correction of Half Width

The azimuthal broadening of the diffraction spot is due to the fluctuation of microcrystals. The precise determination of the half width H_R of diffraction spots is essential for the accurate evaluation of r_χ from eq. (3.5). The experimentally measured

half width H_E includes the instrumental broadening H_I arising from the divergence and width of the impinging X-ray beam. The experimental peak profile is a result of the theoretical profile convolved with the instrumental broadening. Then, we assume

$$H_E^2 = H_R^2 + H_I^2 ,$$

(3.6)

where the instrumental broadening is empirically expressed as a function of the diffraction angle 2θ:

$$H_I = \frac{K}{\sin 2\theta} + \frac{M}{\sin 2\theta},$$

(3.7)

with the K and M terms being the contributions of the beam divergence and the beam width, respectively.

To estimate the validity of eq. (3.7), the calibration of the X-ray diffractometer was performed using L-alanine single crystal. The diffraction spots corresponding to $\{hkl\}$ planes are chosen and the azimuthal half width H_Is for each spot are plotted against its 2θ value. The result is shown in Figure 3.6. The experimental data are fitted by eq. (3.7) with K=0.222 deg and M=0.437 deg as shown by solid line in the figure. The values K and M depend on the instrument used and the camera distance.

Using eqs. (3.5) to (3.7), we obtain

$$H_E^2 = {f_R}^2 (a \sin^2 \Phi_R + b) + \left(\frac{K}{\sin 2\theta} + \frac{M}{\tan 2\theta} \right)^2 .$$

(3.8)

In this equation, the quantities 2θ, f_R^2, and Φ_R^2 are determined for the diffraction spot designated by {*hkl*}.

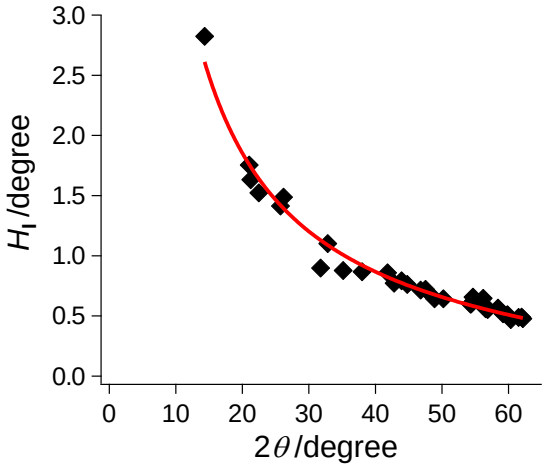

Figure 3.6. The azimuthal half width H_I used for instrumental calibration. The half widths of diffraction spots of L-alanine single crystal are shown as a function of diffraction angle 2θ. The solid line is a fitting performed using Eq. (3.7) with K = 0.222 and M = 0.437.

3.4.3 Determination of r_χ of L-Alanine and D-Mannitol

In Table 3.1, the results are summarized. The unknown parameters a, b, K, and M are determined by least square fitting of the H_E^2 data with respect to the right-hand-side of eq. (3.8). The parameters determined for L-alanine are K=0.10 deg, M=0.33 deg, a=0.54 deg^2, b=0.51 deg^2, and hence r_χ=b/a =1.0. This value is in good agreement with the value determined by the data in literature.[9] The parameters determined for D-mannitol are K=0.22 deg, M=0.26 deg, a=8.69 deg^2, b=10.54 deg^2, and hence, r_χ =b/a =1.2. This value is in good agreement with the value determined by susceptibility data in literature.[10] Using the parameters determined, the corrected half width H_R^2/f_R^2 (eq. (3.5)) is plotted as a function of $\sin^2\Phi_R$ (Figures 3.7(a, b)). A

good linear relationship is obtained.

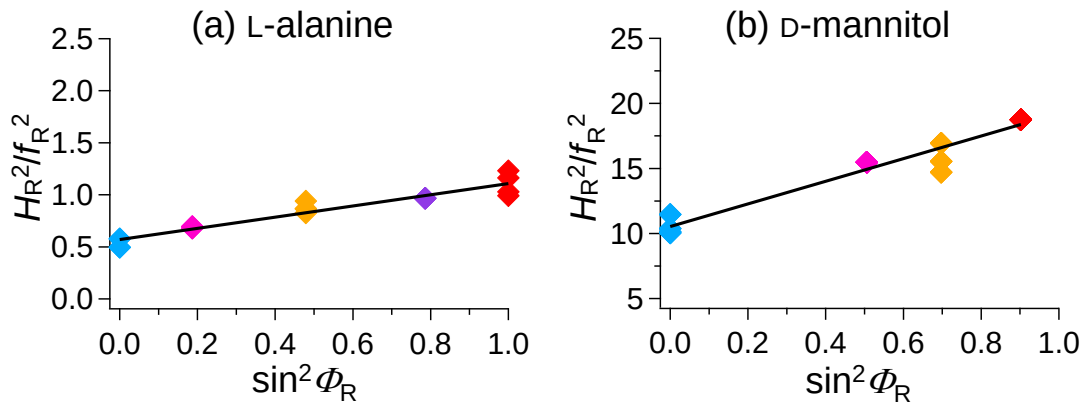

Figure 3.7. The corrected half width H_R^2/f_R^2 (Eq. (3.5)) is plotted as a function of $\sin^2\Phi_R$ for (a) L-alanine and (b) D-mannitol. The slope and intercept of the line is equal to the values *a* and *b*, respectively, from which the anisotropic ratio is determined as $r_\chi=b/a$.

3.4.4 Relationship between r_χ and Orientational Degree of Microcrystals Subjected to Three-Dimensionally Constraining Magnetic Field

As mentioned previously, the square intensity of the orientation fluctuation about each of magnetic axes χ_1, χ_2, and χ_3 is proportional to $(\chi_2-\chi_3)^{-1}$, $(\chi_1-\chi_3)^{-1}$, and $(\chi_1-\chi_2)^{-1}$, respectively. Because of the relation $\chi_1>\chi_2>\chi_3$ by definition, the fluctuation is not isotropic: the magnitude $(\chi_1-\chi_3)^{-1}$ is the smallest in any case, while the magnitude relation between the other two is undetermined. The orientation fluctuation also depends on the applied time-dependent magnetic field.[4,5] It is known that the fluctuations about the χ_1 and χ_3 axes can be equalized by an appropriate choice of the experimental parameters of the time-dependent magnetic field, whereas the fluctuation about the χ_2 axis is the smallest whatever parameters are taken.[4] The parameters that

makes the equalization possible can be determined based on the ratio r_χ of the crystal under consideration. The equalization is important to prepare samples that produce well-resolved X-ray diffraction pattern or exhibit high anisotropic physical properties.

Now we confirm that the value r_χ is useful for determination of the condition of the equalization required for a MOMA sample. Among various types of time-dependent magnetic fields,[4] we used an intermittent sample rotation.[11]

Here we show again the means square fluctuations of the magnetic axes under intermittent magnetic field[4,5]

$$\langle \delta_1^2 \rangle = \frac{C(R+1)}{\chi_2 - \chi_3}, \langle \delta_2^2 \rangle = \frac{C(R+1)}{(2R+1)(\chi_1 - \chi_3)}, \langle \delta_3^2 \rangle = \frac{C(R+1)}{2R(\chi_1 - \chi_2)}. \tag{3.3}$$

These mean square fluctuations are related to the square of the half widths H_{R1}^2, H_{R2}^2, and H_{R3}^2, respectively. The reciprocal lattice vectors corresponding to these half widths are located in the $\chi_2\chi_3$, $\chi_1\chi_3$, and $\chi_1\chi_2$ planes, respectively. The value of H_{R2}^2 is the smallest over the whole range of R because χ_1-χ_3 is the largest. On the other hand, the magnitudes of H_{R1}^2 and H_{R3}^2 depend on the value of R, and become equal at R=(1/2)(χ_2-χ_3)/(χ_1-χ_2)=r_χ/2. Therefore, the value R required for the equalization can be determined if the value r_χ of the crystal is known.

In Figure 3.8, the half widths of the {120}, {011}, and {102} planes of L-alanine MOMA are plotted as a function of R. Because the crystallographic a, b, and c axes of L-alanine coincide with χ_2, χ_3, and χ_1 axes, respectively, the reciprocal lattice vectors corresponding to {120}, {011}, and {102} planes are located on the $\chi_2\chi_3$, $\chi_1\chi_3$, and $\chi_1\chi_2$ planes, respectively. In the same figure, the theoretical half widths H_{R1},

H_{R2}, and H_{R3} corresponding to $H\{120\}$, $H\{011\}$, and $H\{102\}$, respectively, of the L-alanine MOMA are determined using eq. (3.3) and are shown with solid lines, whereby we put $C(\chi_2\text{-}\chi_3)^{-1}=1$, $C(\chi_1\text{-}\chi_3)^{-1}=1/2$, and $C(\chi_1\text{-}\chi_2)^{-1}=1$ because $r_\chi=1.0$ for L-alanine. In addition, the vertical scale is adjusted so as to fit to the experimental data. Though the data are scattered, their tendency is similar to the theoretical lines; $H\{120\}$ increases and $H\{102\}$ decreases with increase in R, while $H\{011\}$ remains almost unchanged. In the case of L-alanine, the equalization is achieved at $R=0.5$ because $r_\chi=1.0$. In fact, from Figure 3.8, we observe that $H\{120\}$ and $H\{102\}$ are close to each other at $R=0.5$.

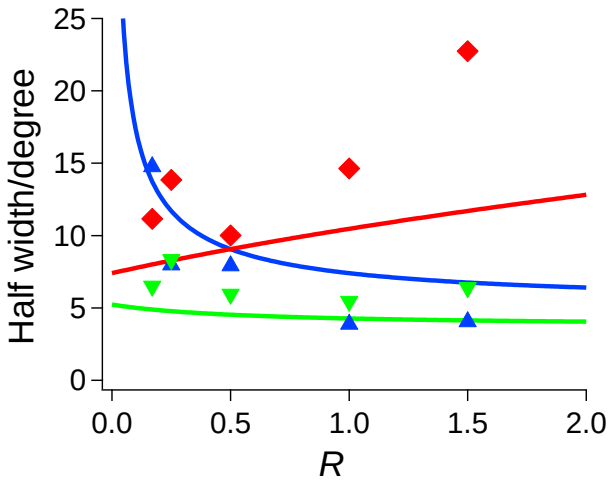

Figure 3.8. The half widths of diffraction spots for the {120} (♦), {011} (▼), and {102} (▲) planes of an L-alanine MOMA plotted as a function of the ratio $R=t_{stop}/t_{rot}$. The half widths of {120}, {011}, and {102} planes correspond to the fluctuations of the reciprocal lattice vectors on $\chi_2\chi_3$, $\chi_1\chi_3$, and $\chi_1\chi_2$ planes, respectively. Red, green, and blue solid lines are the theoretical result for the half widths of $\chi_2\chi_3$, $\chi_1\chi_3$, and $\chi_1\chi_2$ planes, respectively, determined using Eq. (3.3).

3.5 Summary

We determined the ratio r_χ of the diamagnetic anisotropy of L-alanine and D-mannnitol by *in-situ* X-ray diffraction measurements of their microcrystalline suspensions. The results obtained were in good agreement with those estimated by corresponding single crystal data reported in literature. The technique proposed here provides a facile method for determination of the ratio of the magnetic susceptibility from a microcrystalline sample. If the size of microcrystals under investigation is well characterized, the determination of the absolute values of three magnetic susceptibilities is possible.

The ratio r_χ is an important parameter when fabricating MOMAs. We prepared an L-alanine MOMA under various experimental conditions of the time-dependent magnetic field, and found that the ratio r_χ is in fact useful to determine the experimental conditions that make possible the equalization of the half widths of diffraction spots.

Reference

[1] T. Kimura, M. Yoshino, *Langmuir* **2005**, 21, 4805.

[2] T. Kimura, F. Kimura, M. Yoshino, *Langmuir* **2006**, 22, 3464.

[3] M. Yamaki, S. Horii, M. Haruta, J. Shimoyama, *Jpn. J. Appl. Phys*. **2012**, 51, 010107.

[4] M. Yamaguchi, S. Ozawa, I. Yamamoto, T. Kimura, *Jpn. J. Appl. Phys*. **2013**, 52, 013003.

[5] T. Kimura, T. Tanaka, G. Song, K. Matsumoto, K. Fujita, F. Kimura, *Cryst. Growth Des*. **2013**, 13, 1815.

[6] T. Kimura, G. Song, K. Matsumoto, K. Fujita, F. Kimura, *Jpn. J. Appl. Phys*. **2012**, 51, 040202.

[7] H. J. Simpson, R. E. Marsh, *Acta. Cryst*. **1966**, 20, 550.

[8] H. M. Berman, G. A. Jeffrey, R. D. Rosenstein, *Acta. Cryst*. **1968**, B24, 442.

[9] K. Ogawa, Thesis, Iwate University, **2005**.

[10] K. Lonsdale, *Proc. Roy. Soc. London* **1939**, A171, 541.

[11] N. Nakatsuka, H. Yasuda, T. Nagira, M. Yoshiya, *J. Phys. Conf. Ser*. **2009**, 165, 012021

Chapter 4 Single-Crystal Neutron Diffraction Study of Magnetically Oriented Microcrystal Array and Suspension

4.1 Introduction

Neutron crystallographic analysis has the following advantages over X-ray crystallographic analysis: (1) much information on light elements such as hydrogen and lithium can be obtained;[1] (2) isotope can be identified;[2] and (3) direction and magnitude of the magnetic moment of the magnetic atoms be analyzed.[3] However, larger crystals are required for neutron crystallography than for X-ray diffraction measurements, and this is a major hurdle in performing crystallographic analysis.[4] In this study, we employ MOMAs and MOMSs in neutron diffraction measurements and evaluate the possibility of MOMA and MOMS methods for neutron crystallographic analysis using L-alanine as the sample.

Crystallographic studies of L-alanine by X-ray and neutron diffraction have been reported in the literature.[5-8] The L-alanine crystal belongs to the orthorhombic system with a=6.032, b=12.343, and c=5.784 Å, and its space group is $P2_12_12_1$. The c- and b-axes correspond to the easy and hard magnetization axes, respectively.

4.2 Materials and Methods

4.2.1 Preparation of L-Alanine MOMA

As-received L-alanine crystals (Wako Chemical, Ltd.) were pulverized using a mortar and dispersed in an ultraviolet (UV)-curable resin precursor (XVL-14 of Kyoritsu Chemical Co. Ltd.; viscosity of 12 Pa s). The size of microcrystals was between ca. 1 and 60 μm. No special care, such as use of deuterated precursors, was

taken to reduce the background scattering from the resin matrix. The obtained suspension was poured into a plastic container that was 8 mm in diameter and ca. 10 mm in height. The concentration of microcrystals was ca. 17 wt%.

The container was mounted on a sample-rotating unit (Figure 4.1) that was placed in the bore center of a Sumitomo Heavy Industry cryogen-free superconducting magnet generating an 8-T static horizontal magnetic field (the *x*-axis). The rotation axis was vertical (the *z*-axis). Two different frequencies of rotation were applied within one revolution; the rotation frequency was switched between ω_s=40 and ω_q=132 rpm every 90º. This condition was determined from the method described in Chapter 3. The value of r_χ of L-alanine was 1.0. The choice of these rotation speeds, ω_s=40 and ω_q=132, is consistent with the prediction for the best value of $r_\omega=\omega_q/\omega_s$=3.3. The χ'-axis embedded in the sample moves slowly (40 rpm) when it passes through the laboratory *x*-axis that is parallel to the magnetic field. As a result, the χ_1 axis (*c*-axis) aligns parallel to the χ'-axis, and the χ_3 axis (*b*-axis) aligns parallel to the rotation axis (the *z*-axis), resulting in three-dimensional alignment. Experimental and theoretical details are described in chapter 3. Thirty minutes after the sample rotation in a static magnetic field, the suspension was irradiated with UV light for 15 min to photopolymerize the resin precursor. Then, the consolidated specimen was removed from the container to obtain an L-alanine MOMA ca. 8 mm in diameter and 10 mm in height, as shown in Figure 4.2.

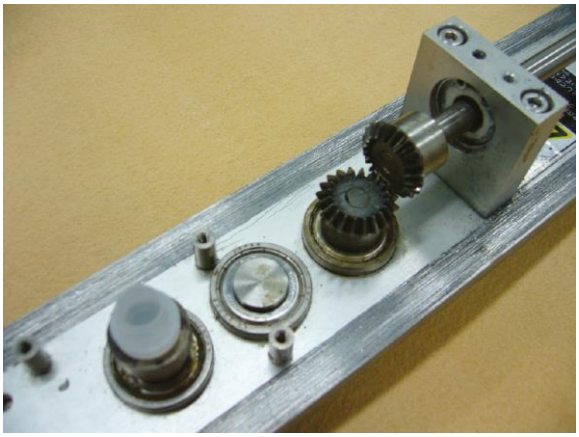

Figure 4.1. Rotating unit used to prepare a magnetically oriented microcrystal array (MOMA). A sample container is mounted on a rotating stage (lower left) that is driven by a stepping motor through bevel gears (top right).

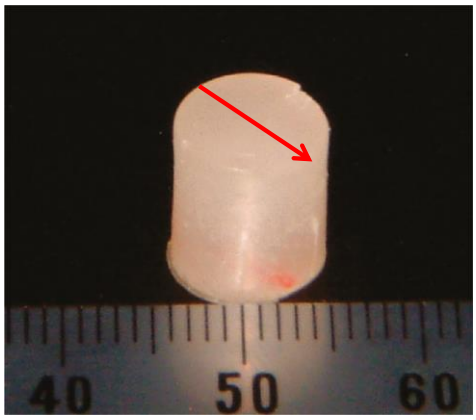

Figure 4.2. Photograph of a magnetically oriented microcrystal array of L-alanine. The crystal is ca. 8 mm in diameter and 10 mm in height. The cylinder axis corresponds to the hard magnetization axis and a red arrow corresponds to the second smallest magnetization axis.

4.2.2 Neutron Diffraction Measurement of L-Alanine MOMA

The neutron diffraction measurements were performed using the double-axis diffractometer MUSASI installed at the T2-3-2 neutron beam port in the guide hole of JRR-3 in Tokai, Japan. The monochromatized beam was set at a wavelength of 2.46 Å with a PG monochromator. Higher-order harmonic contamination was brought down to less than 0.1% by a PG filter. The L-alanine MOMA was mounted on a goniometer

with the (*hk*0) and (*h*0*l*) planes parallel to the horizontal scattering plane. The integrated intensities of 31 independent diffraction spots were measured with a radial scan. These intensities were compared with those calculated using Shelxl-97. Pole figure measurement was also carried out on the same diffractometer with a eulerian cradle attachment. The scattering intensity at the peak position was measured as a function of χ and ϕ angles. The background was removed by subtraction of the baseline.

4.2.3 Fabrication of Rotating System

To apply the MOMS method to neutron diffraction measurements, we built a rotation unit for performing *in-situ* neutron diffraction measurements on a microcrystalline suspension rotating in a magnetic field. Figure 4.3 shows a photograph of the unit. This unit can rotate the suspension in a superconducting magnet. The incident and diffracted neutron beams both pass through the center part of the magnet. This unit made it possible to perform *in-situ* neutron diffraction on a microcrystalline suspension rotating in a magnetic field of up to 10 T.

Figure 4.3. Photograph of a rotating unit (KU model χ10-3). The suspension of a sample is rotated in a superconducting magnet and subjected to *in-situ* X-ray diffraction measurement.

4.2.4 *In-Situ* Neutron Diffraction Measurement of L-Alanine Suspension

L-alanine powder was ground in an agate mortar and filtered through meshes of 125 and 75 μm. 1.05 g of L-alanine powder filtered through the meshes was suspended in 5 ml of PEG#400. A plastic container was tightly filled with the L-alanine suspension.

The superconducting magnet was excited to 1 T. In this 1 T magnetic field, the L-alanine suspension was rotated at 48 rpm and the neutron diffraction of the (040) plane was measured *in-situ*. Similar experiments were performed at 16, 6, and 1 rpm.

4.3 Results and Discussion

4.3.1 Pole Figure (MOMA)

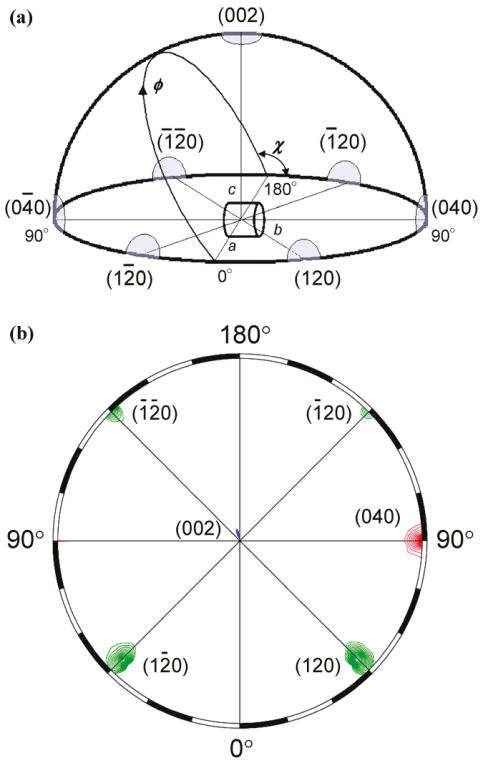

Figure 4.4. (a) Sample setting of the MOMA and the expected diffraction spots. Angle χ runs from 0 to -180° and ϕ runs from 0 to 180°. (b) Pole figure obtained for the MOMA to be compared with (a). Diffraction for (040) was not measured.

In measuring the pole figure, a MOMA sample was set on a goniometer approximately in the direction shown in Figure 4.4(a). The angles χ and ϕ correspond to the operation angles of the goniometer. The angle ϕ runs from 0 to 180º at a given value of the angle χ that runs from 0 to-180^{o}. At this setting, the diffractions corresponding to the (040), (002), (120), etc. are expected to appear at locations shown in the figure. In Figure 4.4(b), the measured pole figure is displayed. Here, all the diffraction spots are displayed in the same figure.

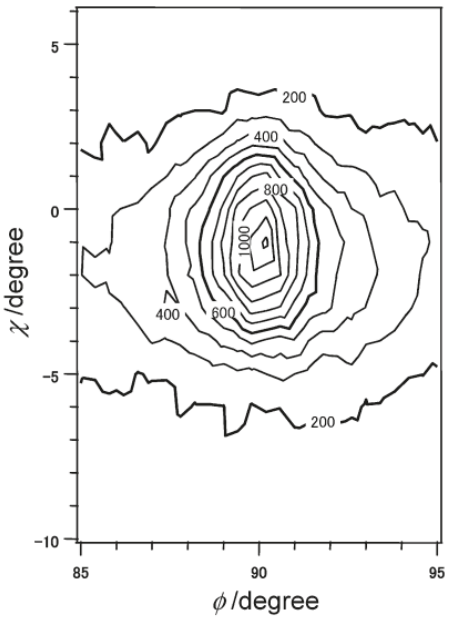

Figure 4.5. Contour plot of the diffraction spot for (040) shown in Figure 4.4(b) as a function of χ and ϕ. Half maximum of the intensity is ca. 600 from which the average half width is estimated to be ca. 4º.

The location of (002) is slightly displaced from χ=-90º and ϕ=90º because the sample was not accurately set as defined in Figure 4.4. A half sphere was scanned so that spots for (120), (120), (120), and (120) were all observed. These spots appear around χ=0, -180^{o} and ϕ=45, 135^{o} because $a/b \approx 1/2$. On the other hand, a spot for (040) was not scanned. Instead, a close examination of (040) was made by scanning in the vicinity of χ=0^{o} and ϕ=90^{o}. A contour plot of the intensity of (040) is shown in Figure 4.5 as a function of χ and ϕ. The average half width over two angles is ca. 4^{o}. The use of a strong magnetic field can help reduce the half width.[11]

A 2θ profile for the (040) diffraction is shown in Figure 4.6 as a typical example. The peak is clearly distinguished from the background. This high signal-to-noise ratio was unexpected because no care was taken to reduce the background incoherent scattering when choosing the resin precursor. This might be attributed to the fact that the coherent diffraction is extremely increased because the microcrystals are aligned three-dimensionally. If there is not a preferential alignment, crystallographic axes, for example, the *a*-axes of microcrystals in a MOMA, are uniformly distributed on a sphere. Then, the probability density is proportional to $(4\pi)^{-1}$. On the other hand, if the *a*-axes are concentrated in a spot with a half width of δ, then the probability density is proportional to $\pi^{-1}(\delta/2)^{-2}$. This indicates that the probability density is magnified by $16\delta^{-2}$ in a MOMA. If δ =0.07 rad (= 4^{o}), for example, then the magnification becomes 3370.

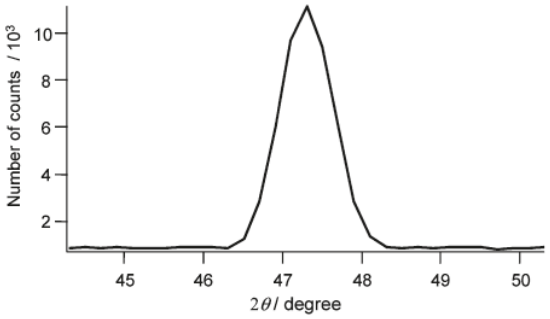

Figure 4.6. Diffraction profile for the (040) plane. Baseline is not subtracted.

4.3.2 Comparison of Observed Intensities of Diffraction Peaks with Calculated Result (MOMA)

After subtraction of the baseline, the intensity of the peak is calculated by integration and corrected for Lorentz factor; no absorption correction was performed. The structure refinement was performed with Shelxl-97 using the crystallographic data of neutron diffraction of L-alanine reported in the literature,[8] where the atom

coordinates, the temperature factors, and the anisotropic temperature factors were fixed. The results are summarized in Table 4.1. The values of $R1$ and $wR2$ are 0.184 and 0.368, respectively.

Table 4.1. Calculated and Measured F^2 Values for Diffractions from (hkl) Planes

hkl			F_c^2	F_o^2
2	0	0	12.86	9.50
4	0	0	10.42	8.69
1	1	0	8.26	7.89
2	1	0	1.02	1.06
3	1	0	0.44	1.43
0	2	0	3.55	5.42
1	2	0	77.06	82.74
2	2	0	3.96	3.58
3	2	0	5.95	3.62
1	3	0	0.26	0.37
2	3	0	1.15	0.89
3	3	0	0.00	−0.43
0	4	0	95.88	167.23
1	4	0	19.92	22.84
2	4	0	0.00	−0.10
1	5	0	8.57	10.76
2	5	0	1.99	0.97
0	6	0	10.09	22.55
1	6	0	8.99	12.59
2	6	0	56.46	33.00
0	8	0	0.42	1.51
3	0	1	13.51	11.27
4	0	1	4.90	2.57
0	0	2	23.59	18.36
1	0	2	23.75	21.53
2	0	2	1.88	2.84
1	0	3	0.06	−0.81
2	0	3	2.53	4.15
3	0	3	2.48	−0.81
0	0	4	14.04	16.37
1	0	4	8.01	7.80

In the present preliminary study, the integration was performed only along the 2θ direction, and the integration with respect to χ and ϕ directions was not performed. In addition, absorption correction was not made. Hence, the intensity data could include some error. However, the experimental and calculated results appear to agree satisfactorily, indicating that the MOMA can provide diffraction data that will lead to a successful structure analysis.

4.3.3 Observation of Diffraction Peaks (MOMS)

The (040) neutron diffraction intensity of the L-alanine suspension rotated at 1, 6, 16, and 48 rpm in a 1 T magnetic field is shown in Figures 4.7(a~d). For rotation speeds of 6, 16, and 48 rpm, clear diffraction peaks were observed. This indicates that the χ_3 axis of the L-alanine microcrystals are oriented in the direction of the rotation axis. However, no clear diffraction peaks were obtained from the suspension rotated at 1 rpm, indicating that the suspension is in the SRR state at 1 rpm. The (040) diffraction spots could not be obtained because the χ_3 axes of the microcrystals are not oriented in the SRR state.

The half width of the peak at 16 rpm is smaller than that at 6 rpm. This is the same result as obtained in Chapter 1, Figure 1.9. However, the half width at 48 rpm is greater than that at 16 rpm probably because centrifugal force increases with increasing rotation speed; this centrifugal force disrupts the orientation. The half width in the (040) plane at 16 rpm was 2.2°, which was well oriented as compared to MOMA. In other words, we successfully obtained clear diffraction peaks by neutron diffraction measurements with the MOMS method as well. However, with the current experiment system, only the (0k0) diffraction peaks can be observed. This method needs to be

improved to enable observation of more diffraction spots.

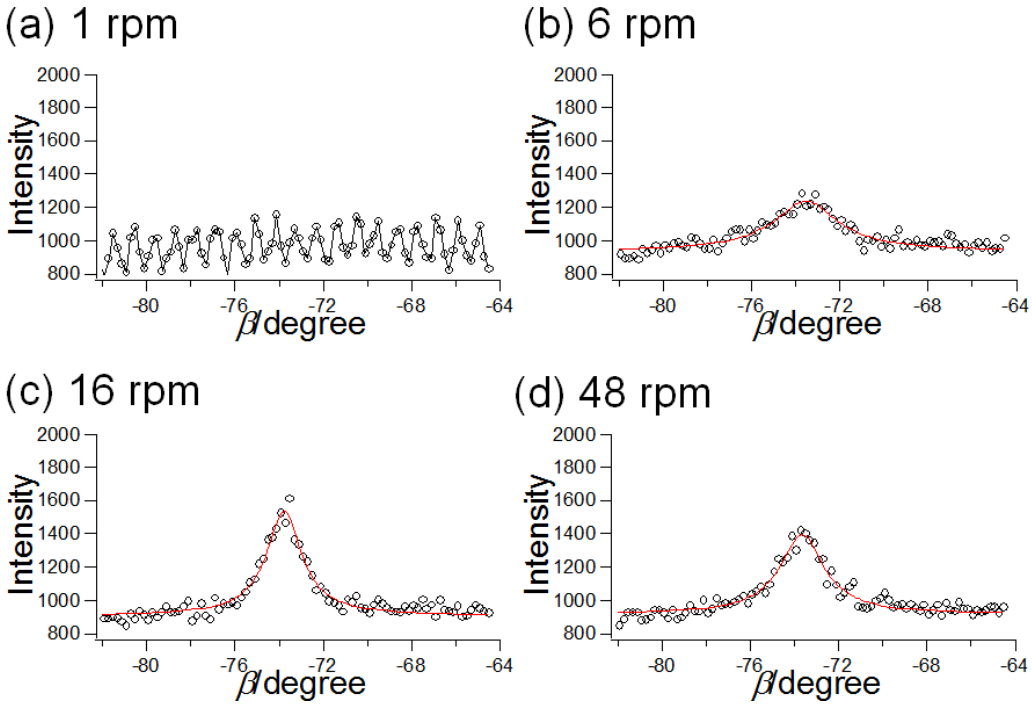

Figure 4.7. Neutron diffraction profiles of β scans around (040) reflection peak of L-alanine suspension rotated in a magnetic field (1 T). The rotation speed was (a) 1 rpm, (b) 6 rpm, (c) 16 rpm, and (d) 48 rpm.

4.4 Summary

To conclude, we have demonstrated the potential of the MOMA and MOMS methods as a powerful means to determine structure by neutron single-crystal analyses. Characteristic features of these methods are summarized as follows: (i) A MOMA and a MOMS are prepared from microcrystalline powder with a particle size as small as tens of micrometers if one uses magnetic fields of 8.0 and 1.0 T, respectively. Microcrystals of even smaller sizes can be used if a stronger magnetic field is applied. (ii) The sample size of a fabricated MOMA can be as large as several millimeters to several centimeters. (iii) The half width of the diffraction spot can be on the order of

4º (MOMA) and 2° (MOMS) under the fabrication conditions employed in the present study. It will be improved if higher magnetic fields are used. (iv) The signal-to-noise ratio on a MOMA method is sufficiently high even though a commercially available resin precursor is used. This is because coherent diffractions from the microcrystals are much higher than the incoherent scattering due to the resin owing to the three-dimensional orientation of microcrystals in the MOMA. Finally, it should be noted that the use of a low temperature resin (STYCAST, GE varnish) as a matrix resin might allow the low temperature measurement with MOMA.

Reference

[1] A. T**.** Brünger, M. Karplus, *Proteins* **1988**, 4, 148.

[2] A. A. Kossiakoff, *Nature* **1982**, 296, 713

[3] J. Rodriguezcarvajal, *Phys*. *B* **1993**, 192, 55.

[4] N. Niimura, *Curr*. *Opin*. *Struct*. *Biol*. **1999**, 9, 602.

[5] H. J. Simpson Jr., R. E. Marsh, *Acta*. *Crystallogr*. **1966**, 20, 550.

[6] M. S. Lehmann, T. F. Koetzle, W. C. Hamilton, *J*. *Am*. *Chem*. *Soc*. **1972**, 92, 2657.

[7] R. Destro, R. E. Marsh, R. Bianchi, *J*. *Phys*. *Chem*. **1988**, 92, 966.

[8] C. C. Wilson, D. Myles, M. Ghosh, L. N. Johnson, W. Wang, *New J*. *Chem*. **2005**, 29, 1318.

[9] K. Ogawa, L. A. Guzman, S. Honjo, J. Imai, N. Doki, K. Shimizu, *J*. *Chem*. *Eng*. *Jpn*. **2006**, 39, 616.

[10] T. Kimura, F. Kimura, M. Yoshino, *Langmuir* **2006**, 22, 3464.

[11] T. Kimura, *Polym*. *J*. **2003**, 35, 823.

General Conclusions

This study was about crystallographic analysis, which is necessary for the advanced use of biomass.

First, in Chapter 1 we discussed *in-situ* X-ray diffraction measurements on a microcrystalline suspension in a static or rotating magnetic field (MOMS method). We obtained fiber diffraction patterns of the microcrystals, where their χ_1 or χ_3 axes are uniaxially oriented in a static or a rotating magnetic field, respectively. In both diffraction patterns, the half width in the azimuthal direction was 2–3°, which represented a very good state of orientation. In the process of obtaining these diffraction patterns, we also determined the orientational behavior of microcrystals in a rotating magnetic field (especially at low to medium speeds). With a low rotation speed (SRR), the χ_1 axis of the microcrystal follows the rotation and remains near the magnetic field. In this case, the χ_2 and χ_3 axes are not oriented. With a medium rotation speed (ARR), the χ_1 axis of the microcrystal rotates and here, the χ_3 axis is oriented in the direction of the rotation axis. When increasing the rotation speed in ARR, the degree of orientation of the χ_3 axis increases to a certain limit. If the half width reaches the limit, it is considered to be rotating at a high speed (RRR).

In Chapter 2, we described a method for performing crystallographic analysis using the two types of fiber diffraction patterns obtained in Chapter 1. First, we proposed a method for effortlessly performing indexing (including the determination of the crystal system, lattice constant, and space group), which is often difficult but necessary for powder crystallographic analysis, and verified its usefulness using L-alanine. Furthermore, we compared the intensity of the 44 obtained independent

diffraction peaks with the calculated value. We obtained the result $R1$=0.188, $wR2$=0.463, and showed the possibility of crystallographic analysis based on the MOMS method.

In Chapter 3, from the two types of fiber diffraction patterns obtained in Chapter 1, we determined the substance-specific value r that is required for three-dimensional magnetic field orientation of the microcrystals. In this experiment, using L-alanine and D-mannitol as samples, we obtained the values r_{χ}=1.0, 1.2, which were close to the literature data. There were substances for which magnetic field orientation was difficult because their magnetic susceptibilities were unknown, but the above result made determining the optimal three-dimensional orientation for these substances possible. This could strongly contribute to development of the MOMA method.

In Chapter 4, we evaluated the possibility of applying the MOMA and MOMS methods to neutron crystallographic analysis. For MOMA, clear diffraction spots were obtained from a neutron diffraction measurement similar to an X-ray diffraction measurement. Comparing the measured intensity with the calculated value, $R1$ and $wR2$ were 0.184 and 0.368 respectively, and we demonstrated the possibility of applying the MOMA method to neutron crystallographic analysis. Similarly, clear diffraction spots were observed by neutron diffraction measurements of MOMS, suggesting the potential for this type of crystallographic analysis.

Next, we discuss future prospects based on this study. There are two possible directions that crystallographic analysis using the MOMS method can take. One is to perform both indexing and refinement from the two types of fiber diffraction patterns. The other is to perform indexing alone from the two types of fiber diffraction patterns

and then use a powder diffraction method such as the Rietveld method for the refinement. The latter has an advantage over the former; it avoids complex calculations for comparing diffraction intensities between the two diffraction patterns. Additionally, it is similar to the existing methods of powder crystallographic analysis; therefore, it will be easy to apply in actual use. However, the former is more likely to be eventually capable of accurate structure refinement.

As X-ray crystallographic analysis improves, the advantages of neutron crystallographic analysis will become less prominent. However, since isotope structures cannot be determined by X-rays in principle, the neutron diffraction measurement is still advantageous in this case. Therefore, when applying the MOMA and MOMS methods to neutron crystallographic analysis, we should focus on samples that have characteristic isotope structures.

Finally, slightly off-topic from structural analysis but progressing from the study in Chapter 3, we mention a method for determining magnetic susceptibility from a microcrystal sample. Similar to the crystal structure, the magnetic susceptibility cannot be determined without a large single crystal. For a biaxial crystal, there are three magnetic susceptibilities χ_1, χ_2 and χ_3. In Chapter 3, we introduced a method for determining the anisotropy ratio $r_\chi (=(\chi_2-\chi_3)/(\chi_1-\chi_2))$ of the magnetic susceptibility of the crystal. The magnetic susceptibility of a powder sample is relatively easy to measure, and the value obtained from this measurement is the average of the three magnetic susceptibilities: $(\chi_1+\chi_2+\chi_3)/3$. Here, if there is another linear equation with respect to magnetic susceptibility, the values of the three magnetic susceptibilities can be determined. SQUID measurements of the microcrystalline suspension could help obtain this equation. When measuring the microcrystalline suspension with a SQUID,

the χ_1 axis of the microcrystal becomes uniaxially oriented in the direction of the magnetic field in the SQUID. As a SQUID measures magnetization components in the direction of the magnetic field, this measuring method can be used to determine the value of χ_1 of the crystal. Using this value of χ_1 with the two previously obtained equations, it is possible to determine all values of the magnetic susceptibilities.

List of Publication

The contents of this thesis have been described in the following publications.

Original Papers

1. ‘‘Single-Crystal Neutron Diffraction Study of Pseudo Single Crystal Prepared from Microcrystalline Powder’’, Fumiko Kimura, Tsunehisa Kimura, Kenji Matsumoto, and Naoto Metoki, *Cryst. Growth & Des.* **2010**, 10, 48 (**Chapter 4**)

2. ‘‘X-ray Diffraction of a Magnetically Oriented Microcrystal Suspensionof L-Alanine’’, Kenji Matsumoto, Fumiko Kimura, Shu Tsukui, and Tsunehisa Kimura, *Cryst. Growth & Des.* **2011**, 11, 945 (**Chapter 1**)

3. **‘‘**Determination of anisotropic magnetic susceptibility by *in situ* X-ray diffraction measurement of orientational fluctuation of microcrystalline suspension under magnetic field**’’,** Kenji Matsumoto, Keiji Fujita, Tatsuya Tanaka, Fumiko Kimura, and Tsunehisa Kimura, *Jpn. J. Appl. Phys*, in submission (**Chapter 3**)

4. ‘‘A Facile Method to Determine Crystal System of Microcrystalline Powder by Using Magnetically Oriented Microcrystal Suspension’’, Kenji Matsumoto, Fumiko Kimura, Guangjie Song, Shuhei Yamane, Shingo Higuchi, and Tsunehisa Kimura, *Cryst. Growth & Des.*, to be submitted (**Chapter 2**)

International Conference

1. ‘‘X-ray diffraction from magnetically aligned microcrystalline powder’’, Kenji Matsumoto, Fumiko Kimura, and Tsunehisa Kimura, *PACIFICHEM2010*, Honolulu, Hawaii, The USA, December, 2010.

2. ‘‘Magnetic anisotropy of diamagnetic crystal examined by X-ray diffraction’’, Kenji Matsumoto, Fumiko Kimura, and Tsunehisa Kimura, *REMT2011*, Kyoto, Japan, September, 2011.

3. ‘‘Crystal Structure Analysis by *In-situ* X-ray Diffraction Measurement of Magnetically Oriented Microcrystal Suspension’’, Kenji Matsumoto, Fumiko Kimura, and Tsunehisa Kimura, *ICMS2013*, Bordeaux, France, October, 2013.

Book Chapters

1. ‘‘Magnetically oriented microcrystal array: A large sample for neutron diffraction analysis’’, Tsunehisa Kimura, Fumiko Kimura, Kenji Matsumoto, and Naoto Metoki, *Neutron Diffraction*, Edited by Dr Irisali Khidirov, Intech, 2012.

Patent

1. ‘‘Method and analysis apparatus of structure analysis of microcrystalline powder’’, Inventors: Tsunehisa Kimura, Fumiko Kimura, and Kenji Matsumoto, Applicant: *Kyoto University*, Application number: 2013-265882.

Other publications of the author based on the work at Laboratory of Fibrous Biomaterials, Division of Forest and Biomaterials Science, Graduate School of Agriculture, Kyoto University are specified below.

1. ‘‘Determination of Anisotropic Diamagnetic Susceptibility Using X-ray Diffraction’’, Tsunehisa Kimura, Guangjie Song, Kenji Matsumoto, Keiji Fujita, and Fumiko Kimura, *Jpn. J. Appl. Phys.* **2012**, 51, 040202.

2. ‘‘Determination of Ratio of Diamagnetic Anisotropy of a Biaxial Crystal by X-ray Diffraction Measurement’’, Guangjie Song, Kenji Matsumoto, Keiji Fujita, Fumiko Kimura, and Tsunehisa Kimura, *Jpn. J. Appl. Phys.* **2012**, 51, 060203.

3. ‘‘Orientation Fluctuation of Microcrystals under Three-Dimensionally Constraining Dynamic Magnetic Fields’’, Tsunehisa Kimura, Tatsuya Tanaka, Guangjie Song, Kenji Matsumoto, Keiji Fujita, and Fumiko Kimura, *Cryst. Growth & Des.* **2013**, 13, 1815.

Other international presentation of the author based on the work at Laboratory of Fibrous Biomaterials, Division of Forest and Biomaterials Science, Graduate School of Agriculture, Kyoto University is specified below.

1. ‘‘In-situ X-ray Diffraction Measurements Using Magnetically Oriented Microcrystal Suspension of L-Alanine’’, Fumiko Kimura, Kenji Matsumoto, Chiaki Tsuboi, Shu Tsukui, and Tsunehisa Kimura, *ICMS2013*, Bordeaux, France, October, 2013.

Acknowledgments

The present thesis is based on the studies which the author has carried out in Laboratory of Fibrous Biomaterials, Division of Forest and Biomaterials Science, Graduate School of Agriculture, Kyoto University, from 2008 to 2014, under the guidance of Professor Tsunehisa KIMURA.

The author would like to express his sincerest gratitude to Professor Tsunehisa KIMURA for his excellent navigation, invaluable suggestions and assistance, and continuous encouragement during the entire course of this work. A sequence of studies in the present thesis would not have been possible to accomplish without his warmest and kindest acceptance as a doctoral student.

The author is deeply grateful to Professor Yoshiyuki NISHIO and Professor Toshiyuki TAKANO, Division of Forest and Biomaterials Science, Graduate School of Agriculture, Kyoto University, for their critical readings of the manuscript and valuable suggestions.

The author wishes to express his gratitude to Assistant Professor Ryosuke KUSUMI and Dr. Fumiko KIMURA, Division of Forest and Biomaterials Science, Graduate School of Agriculture, Kyoto University, for their helpful suggestions and comments.

The author acknowledges Dr. Naoto METOKI, Advanced Science Research

Center, Japan Atomic Energy Agency, for his hard cooperation of the neutron diffraction observations. The author wishes to express his thanks to Assistant Professor Atsushi KITADA, Division of Materials Properties, Graduate School of Engineering, Kyoto University, for his kind cooperation of the SQUID measurements.

The author wishes to thank all the members in the Laboratory of Fibrous Biomaterials for their kind help in many ways.

Last but not least, the author's appreciation goes to his whole family for their never-ending support and continuous encouragement.

January 2014

Kenji MATSUMOTO